The pathologies associated with functional titration of phosphatidylinositol transfer protein α activity in mice

James G. Alb, Jr.,* Scott E. Phillips,* Lindsey R. Wilfley,† Benjamin D. Philpot,†,§, and Vytas A. Bankaitis[1],***

Department of Cell and Developmental Biology, Lineberger Comprehensive Cancer Center,* Department of Cell and Molecular Physiology,† Neuroscience Center,§ Neurobiology Curriculum,** University of North Carolina at Chapel Hill, Chapel Hill, NC 27599-7090

Abstract Phosphatidylinositol transfer proteins (PITPs) bind phosphatidylinositol (PtdIns) and phosphatidylcholine and play diverse roles in coordinating lipid metabolism/signaling with intracellular functions. The underlying mechanisms remain unclear. Genetic ablation of PITPα in mice results in neonatal lethality characterized by intestinal and hepatic steatosis, spinocerebellar neurodegeneration, and glucose homeostatic defects. We report that mice expressing a PITPα selectively ablated for PtdIns binding activity (Pitpα^{T59D}), as the sole source of PITPα, exhibit phenotypes that recapitulate those of authentic PITPα nullizygotes. Analyses of mice with graded reductions in PITPα activity reveal proportionately graded reductions in lifespan, demonstrate that intestinal steatosis and hypoglycemia are apparent only when PITPα protein levels are strongly reduced (≥90%), and correlate steatotic and glucose homeostatic defects with cerebellar inflammatory disease. Finally, reconstitution of PITPα expression in the small intestine substantially corrects the chylomicron retention disease and cerebellar inflammation of *Pitpα*$^{0/0}$ neonates, but does not rescue neonatal lethality in these animals. These data demonstrate that PtdIns binding is an essential functional property of PITPα in vivo, and suggest a causal linkage between defects in lipid transport and glucose homeostasis and cerebellar inflammatory disease. Finally, the data also demonstrate intrinsic neuronal deficits in PITPα-deficient mice that are independent of intestinal lipid transport defects and hypoglycemia.—Alb, J. G., Jr., S. E. Phillips, L. R. Wilfley, B. D. Philpot, and V. A. Bankaitis. **The pathologies associated with functional titration of phosphatidylinositol transfer protein α activity in mice. *J. Lipid Res.* 2007.** 48: **1857–1872.**

Supplementary key words signaling • phospholipids • lipoproteins • neurodegeneration

The physical compartmentation of signal transduction to specific microdomains of membrane surfaces is a common property of all eukaryotic cells, and various mechanisms are applied toward achieving this end (1–5). One such mechanism involves the spatially and temporally regulated metabolic channeling of phosphatidylinositol (PtdIns) and/or phosphatidylcholine (PtdCho) monomers by phosphatidylinositol transfer proteins (PITPs). This PITP-mediated channeling is itself linked to specific physiological outcomes (6–8). Prime among these are the roles of PITPs in coordinating various interfaces between lipid metabolism and membrane trafficking reactions. PITPs fall into two unrelated structural classes: the Sec14-like PITPs and the so-called class 1 metazoan PITPs (9–12). The Sec14-like PITPs are better understood because detailed functional analyses have been more accessible for these proteins. The metazoan PITPs are poorly characterized from a functional point of view.

Mammals express four known class 1 PITP forms: PITPα, PITPβ, an alternative spliceoform of PITPβ, and rdgBβ (13–18). Data that address in vivo functions for PITPα and PITPβ are building. These proteins are encoded by distinct genes but are highly similar, sharing 77% and 95% primary sequence identity and similarity, respectively. The extensive homology notwithstanding, available data suggest that PITPα and PITPβ execute distinct roles in mammals. First, these proteins exhibit distinct intracellular distributions. PITPα represents a cytosolic/nuclear protein, whereas PITPβ is localized predominantly to the *trans*-Golgi network of mammalian cells [as is its alternative spliceoform (17)]. Second, PITPβ binds the ceramide-based phospholipid sphingomyelin, whereas PITPα does not (15, 17, 19). Finally, the consequences of the genetic ablation of each protein are different (20, 21). The functional nonredundancy of PITPα and PITPβ conforms to the general theme that PITPs are tightly coupled to specific physiological functions in cells (6–8). How PITPs couple

Manuscript received 23 March 2007 and in revised form 11 May 2007.

Published, JLR Papers in Press, May 24, 2007.
DOI 10.1194/jlr.M700145-JLR200

Abbreviations: CRD, chylomicron retention disease; ER, endoplasmic reticulum; EtOH, ethanol; fEPSP, field excitatory postsynaptic potential; GFAP, glial fibrillary acidic protein; MAMA, mismatch amplification mutation assay; PAC, P1 artificial chromosome; PITP, phosphatidylinositol transfer protein; PtdCho, phosphatidylcholine; PtdIns, phosphatidylinositol; TG, triglyceride.

[1] To whom correspondence should be addressed.
e-mail: vytas@med.unc.edu

individual PtdIns and PtdCho binding activities to biological functions remains to be determined.

Genetic ablation of the PITPα structural gene in mice has interesting consequences. *Pitpα*$^{0/0}$ progeny develop to term, but expire within several days after birth from a complex disease course that includes defects in dietary fat and α-tocopherol transport from the small intestine [chylomicron retention disease (CRD)], liver steatosis, hypoglycemia, inflammation of cerebellum and hindbrain, and spinocerebellar neurodegenerative disease (21). These pathologies raise a number of questions. First, which biochemical properties of PITPα are relevant for in vivo function (i.e., are the PtdIns and PtdCho binding activities differentially used in vivo, or are these themselves coupled?). Second, which of these pathologies are causally linked, and which derive from independent insults? It is suggested the intestinal defects and hypoglycemia are linked, and that these defects provoke the cerebellar and hindbrain neurodegenerative diseases (21). Resolution of these questions is key to an understanding of PITPα function in mammalian systems.

Here, we show that PtdIns binding is an essential functional property of PITPα in mammals. It is further demonstrated that intestinal steatosis and hypoglycemia require manifest reductions in PITPα activity, and that these pathologies correlate with cerebellar inflammatory disease. Finally, the data indicate that reconstitution of PITPα expression in the small intestine alleviates the CRD and cerebellar inflammatory disease of *Pitpα*$^{0/0}$ neonates, but fails to effectively rescue the neonatal lethality of these animals. This failure is accompanied by exacerbations in microvesicular steatosis of the liver, a result consistent with the idea that PITPα regulates the trafficking of luminal lipid cargos.

MATERIALS AND METHODS

Mouse genotyping

Wild-type and *Pitpa::NEO* alleles were diagnosed from tail clip genomic DNA templates using a three-primer PCR assay described previously (21). To screen for the *vibrator* allele (*Pitpα*^{vb}), a hypomorphic mutation that reduces the expression of wild-type PITPα by ~80%, an intracisternal A particle retrotransposon three-primer PCR assay was used (22). The allele-specific forward primers for the wild-type and *vibrator* alleles were Ham-For (5′-AGTGATCGGGACTTTTGTTTCC-3′) and intracisternal A particle retrotransposon-1 (5′-AACGCGTCTAATAACACTTGTG-3′), respectively. A common reverse primer was used, Ham-Rev (5′-CCAAAAGGACTGCCCAGTCATTTTTCCCC-3′). The *vibrator* primer sequences were provided courtesy of Bruce Hamilton (University of California at San Diego).

To generate a *PITPα* transgene whose expression is limited to the duodenum, plasmid *pNSE-EX4* (23) (a gift of Greg Cox, Jackson Laboratories, Bar Harbor, ME) was cleaved with *Xho*I to remove the existing neuronal enolase promoter, and the intestinal fatty acid binding promoter (P_{IFABP}) (24) was introduced in its stead. The *PITPα* open reading frame cDNA was generated by PCR as a 5′-*Hind*III-*Eco*RI-3′ fragment and correspondingly subcloned into the P_{IFABP}-pNSE-EX4 vector to yield plasmid *pFabpiPITPα*. The resultant plasmid was linearized by digestion with restriction endonuclease *Sal*I and injected into C57BL/6J×C3H hybrid pronuclei at the University of North Carolina Animals Model Core to generate transgenic murine founder lines. Transgenic founders were identified with a *PITPα* cDNA-specific set of primers: Alpha-For (5′-GCAAAGTTCCCACGTTTGTTCG-3′) and Alpha-Rev (5′-CTCTTGCTTATGTATAAAGTTTTCC-3′). These primers support the synthesis of a diagnostic 450 bp PCR product. Three independent founders were crossed to C57BL/6J *PITPα*$^{+/0}$ mice to generate *Pitpα*$^{+/0}$*;Tg(*P_{IFABP}*::PITPα)* lines.

Generation of a PtdIns binding-deficient PITPα transgene

Escherichia coli strain DY380 was transformed with P1 clone 4232 (a gift from Bruce Hamilton, University of California at San Diego), which contains the entire *PITPα* genomic locus in a P1 artificial chromosome (PAC) vector harboring a kanamycin resistance selection marker, to generate *E. coli* strain DY380-*Tg(PITPα)*. DY380 is permissive for homologous recombination when electroporated linear double-stranded DNA is introduced into this *E. coli* host (25, 26). The T59D missense substitution was incorporated into exon 3 of the *PITPα* gene as follows. A pair of 100mer oligonucleotides precisely complementary to each other in their respective 3′ 20 nucleotides was constructed. The 20 bp complementary regions spanned the threonine 59 codon, which was converted during oligonucleotide synthesis from the wild-type ACA nucleotide sequence to GAG (and the corresponding reverse complement). Oligonucleotides were annealed at 42°C for 1 h, and the remaining 3′ recessed ends were filled in with Klenow fragment of DNA polymerase I (Promega, Madison, WI). The resultant 200 bp linear double-stranded DNA fragment represented the targeting cassette for incorporating the T59D missense mutation into exon 3 of the *PITPα* structural gene.

The 200 bp target fragment was electroporated into DY380-*Tg(PITPα)* cells prechallenged at 42°C for 15 min (to induce the recombineering machinery), transformants were selected in Luria broth supplemented with kanamycin (50 μg/ml), survivors were serially diluted into five 96-well culture plates to a density of ~10 colony-forming units per well, and the individual pools were expanded. Aliquots from each well were collected and corresponding DNA templates were prepared for screening using a mismatch amplification mutation assay (MAMA) PCR. MAMA-PCR used a forward primer (5′-GGCGAGAAAGGCGAGTACGAG-3′) specific for the mutant T59D codon (underlined) and reverse primer (5′-CTCACATGCCACACACTCC-3′) that hybridizes to sequences within the *PITPα* gene not represented in the original 200 bp targeting fragment. Aliquots yielding a 300 bp PCR product diagnostic of *Pitpα*^{T59D} clones identified the wells of interest, and the corresponding well cultures were subjected to limit dilution and plated for single colonies. Individual colonies derived from well pools of interest were rescreened by MAMA-PCR. Positive clones yielded candidate purified P1 *Tg(Pitpα*^{T59D} clones. Identities were verified by nucleotide sequence analysis of *PITPα* exon 3 of individual candidates. We estimate a 1:12,000 ratio of *Tg(Pitpα*^{T59D}*)* to *Tg(PITPα)* in the final pools.

Immunoblotting and ELISA

Whole mouse brains or duodenal sections were solubilized in RIPA buffer (50 mM Tris-HCl, pH 7.2, 1.0% Nonidet P-40, 0.1% SDS, 0.15 mM NaCl, and 1× protease inhibitor cocktail tablet; Roche, Indianapolis, IN). Protein was estimated using BCA (Pierce, Rockford, IL) for purposes of normalization in immunoblot and ELISA experiments. For immunoblotting experiments, 75 μg of brain lysate was resolved by SDS-PAGE and transferred to nitrocellulose membrane (Bio-Rad Laboratories, Hercules, CA). Membranes were subsequently decorated with PITPα-specific antibody as described previously (20), and with a β-actin specific antibody (Oncogene, Carpinteria, CA) for purposes of normalization. For

ELISA analyses, serial amounts of brain lysate protein for each experimental sample (1 μg, 100 ng, and 10 ng) were coated, in duplicate, on 96-well plastic plates. Samples were dried overnight, washed in 0.5% Tween 20, blocked with 2% BSA, incubated with the appropriate primary antibody overnight at room temperature, washed in PBS, incubated with secondary antibody, and finally developed using *o*-phenylenediamine reagent (Sigma, St. Louis, MO).

Blood chemistry

Whole blood was collected from mice immediately after decapitation or via heart puncture (in 2 mM EDTA, pH 7.2, final concentration for plasma), clotted, and clarified by low-speed centrifugation. Serum glucose was determined by the Trinder assay (Sigma). Plasma triglyceride (TG) measurements were performed on 30 μl plasma aliquots at the Animal Clinical Chemistry and Gene Expression Laboratories at the University of North Carolina-Chapel Hill. Agarose electrophoresis of whole serum used the Titan Gel Lipoprotein Kit (Helena Laboratories, Beaumont, TX) according to the manufacturer's specifications. Resolved samples were developed by staining of gels in 0.1% Fat Red 7B (w/v) in 95% methanol. Chylomicron densities were determined by scanning dried Titan gels using a Bio-Rad VersaDoc imaging system (525 nm) and quantified by the Quantity One software package.

Whole carcass analyses

Carcass compositional analyses were performed as described (21). Briefly, eviscerated carcasses were weighed and body water content determined after drying. Dried carcasses were ground to homogeneity and extracted with petroleum ether in a Soxhlet apparatus to determine fat mass and fat-free dry mass. Carcass ash was measured after limit incineration of fat-free dry mass material.

Histological methods

Mice were prepared for all analyses by anesthesia with 1.25% Avertin (Sigma) and fixed by heart perfusion with sequential phosphate-buffered saline and 4% paraformaldehyde solutions. Intestines, brains, and livers were harvested, intestines were flushed with fixative, and all tissues were postfixed in 4% paraformaldehyde for 24 h. When dehydration was required, tissues were embedded in paraffin, and 5 μm thick sections were cut and mounted onto slides. When frozen samples were required, tissues were embedded in OCT, and 12 μm thick sections were cut and mounted.

For intestinal and liver staining with osmium (27), paraffin sections were rehydrated in a step series starting with xylene and terminating with 50% ethanol (EtOH) (i.e., xylene, 95% EtOH, 90% EtOH, 80% EtOH, 70% EtOH, 60% EtOH, and 50% EtOH), stained for total lipid by incubation with 5% potassium dichromate and 2% OsO_4 for 8 h, and counterstained with toluidine blue O. Samples were then dehydrated in a 50% EtOH-to-xylene series that was the reverse of the rehydration series described above. Dehydrated sections were mounted in Permount (Fisher Scientific, Atlanta, GA). Oil Red O staining was used to identify neutral lipid (27). Frozen sections mounted onto slides were incubated in 85% propylene glycol, stained with Oil Red O, counterstained with hematoxylin, and mounted in glycerol.

For whole brain analyses, fixed samples were washed for several days in phosphate-buffered saline. Brains were then sliced in half along the sagittal plane and embedded in paraffin, and 5 μm-thick sections were cut. Sections were rehydrated as described above and incubated with anti-glial fibrillary acidic protein (GFAP) antibody (EMD Biosciences CalBiochem, San Diego, CA). Decorated slices were developed with the Vectastain ABC kit (Vector Laboratories, Burlingame, CA), followed by counterstaining with toluidine blue. Samples were finally dehydrated in xylene/EtOH (50%) and mounted in Permount (Fisher Scientific).

α-Tocopherol measurements

Whole brains were harvested from decapitated mice, and α-tocopherol was extracted with chloroform as described (21). Samples were resolved by HPLC using a Perkin-Elmer Life Sciences model LC200 gradient pump with an AS 200 Autosampler and an LC 295 ultraviolet-visible light detector.

Liver glycogen analysis

Whole livers were extracted from euthanized animals and homogenized, and glycogen was recovered by acid extraction (28). Recovered material was quantitatively hydrolyzed to glucose by amyloglucosidase, and released glucose was quantified by Trinder assay (Sigma).

Hippocampal field excitatory postsynaptic potential recordings

Age-matched (P4–P6) *PITPα*$^{+/+}$ and *Pitpα*$^{0/0}$ mice were anesthetized with an overdose of pentobarbital barbiturate and decapitated upon the disappearance of corneal reflexes, in compliance with U. S. Department of Health and Human Services and University of North Carolina guidelines. Brains were dissected immediately, and dorsal hippocampi were cut in 400 μm coronal slices in ice-cold oxygenated dissection buffer (75 mM sucrose, 87 mM NaCl, 2.5 mM KCl, 1.25 mM NaH_2PO_4, 26 mM $NaHCO_3$, 10 mM glucose, 7 mM $MgCl_2$, 0.5 mM $CaCl_2$, and 1.3 mM ascorbic acid). Hippocampal slices were equilibrated for 30 min in a submersion chamber at 35°C filled with artificial cerebrospinal fluid (124 mM NaCl, 3 mM KCl, 1.25 mM Na_2PO_4, 26 mM $NaHCO_3$, 1 mM $MgCl_2$, 2 mM $CaCl_2$, and 20 mM D-glucose, saturated with 95% O_2 and 5% CO_2; ~315 mOsm and pH ~ 7.25) and then held at room temperature until use. For recordings, hippocampal slices were placed in an interface chamber, maintained at 31°C, and perfused with oxygenated artificial cerebrospinal fluid. Synaptic responses were evoked by stimulating the Schaffer collaterals with a bipolar stimulating electrode (FHC, Inc., Bowdoin, ME), and field excitatory postsynaptic potentials (fEPSPs) were recorded in stratum radiatum of the CA1 region. Input-output curves were generated by systematically varying the stimulation intensity and measuring the fEPSP slope. Fiber volley amplitude was compared with the fEPSP slope to relate presynaptic to postsynaptic responses. The paired-pulse facilitation of the fEPSP slope and amplitude was examined by adjusting the stimulation intensity to the half-maximal response and systematically varying the interstimulus interval between two stimulations. Statistical analyses used a multivariate two-way ANOVA, with significance placed at $P < 0.05$.

RESULTS

A murine strain that exclusively expresses a PtdIns binding-deficient PITPα

PITPα binds/exchanges PtdIns and PtdCho monomers between membrane bilayers in vitro. It is not yet established what each individual activity contributes to PITPα action in cells. The availability of mutant PITPα derivatives with selective defects in PtdIns binding (29), and the ability to generate PITPα nullizygous (*Pitpα*$^{0/0}$) mice with outstanding phenotypes (21), permit experimental assay of the contribution of PtdIns binding to PITPα function

in the mammal. To this end, the mutant Pitpα^{T59D} was used to assess the in vivo consequences of inactivating PITPα PtdIns binding activity. Residue threonine 59 is required for coordination of the inositol headgroup of PtdIns, and the introduction of any residue bulkier than threonine at this position evokes a selective steric incompatibility with PtdIns binding (**Fig. 1**) (10, 29, 30). Because choline is less bulky than inositol, PtdCho binding is unaffected in Pitpα^{T59D}.

The strategy used for generating mice that express only Pitpα^{T59D} involved recombineering-mediated site-directed mutagenesis of a 76 kDa PAC containing the entire *PITPα* genomic locus. This PAC [henceforth referred to as *Tg(PITPα)*] was shown previously to phenotypically complement the hypomorphic PITPα *vibrator* mutation (22). As a control for all subsequent experiments, we tested whether *Tg(PITPα)* also rescues *Pitpα$^{0/0}$* lethality. Indeed, *Tg(PITPα)* efficiently complements all *Pitpα$^{0/0}$*-associated phenotypes. *Pitpα$^{0/0}$;Tg(PITPα)* animals are long-lived (the oldest animals are 16 months of age at present and healthy), are fertile, and are phenotypically *PITPα$^{+/+}$* in all obvious respects (data not shown). Thus, the *Tg(PITPα)* vector is a suitable precursor for the expression of mutant forms of PITPα in the mouse for functional studies.

The *PITPα* PAC mutagenesis scheme is outlined in **Fig. 2A**. The *Pitpα^{T59D}* PAC [referred to as *Tg(Pitpα^{T59D})*] was injected into C57BL/6J×C3H hybrid pronuclei to generate founder mice. Standard mating strategies were used to generate *PITPα$^{+/0}$;Tg(Pitpα^{T59D})* parental lines from which *Pitpα$^{0/0}$;Tg(Pitpα^{T59D})* progeny were derived. The presence of *Tg(Pitpα^{T59D})* was diagnosed by probing for DNA sequences unique to the bacterial plasmid backbone of this vector (Fig. 2B) (see Materials and Methods). However, because an intact 76 kDa *PITPα* locus was used as the mutagenesis substrate, diagnostic assays for *Tg(Pitpα^{T59D})* were more complicated. Additional methods were required to independently confirm mouse genotypes (see below). To that end, a robust MAMA-PCR strategy that distinguishes the endogenous *PITPα* locus from ectopic *Tg(Pitpα^{T59D})* was developed for purposes of diagnostic genotyping of transgenic mice (see Materials and Methods) (Fig. 2B). Demonstration that this assay reliably detects *Pitpα^{T59D}* in genomic DNA preparations is shown in Fig. 2C.

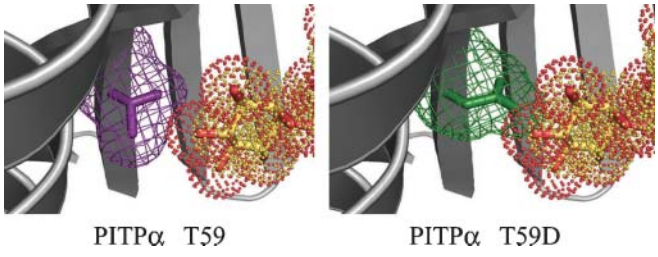

Fig. 1. Residue threonine 59 (T59) and phosphatidylinositol transfer protein α (PITPα)-mediated phosphatidylinositol (PtdIns) binding/exchange activity. Left panel: The van der Waals space of PITPα residue threonine 59 is depicted in mesh mode (violet), whereas the van der Waals space of the inositol ring of bound PtdIns is rendered in dot mode (red and yellow). Note how closely the threonine 59 side chain abuts inositol ring space. Right panel: Same as the left panel except an aspartate side chain is modeled for threonine at PITPα residue 59 to depict the T59D missense mutation. The aspartate 59 van der Waals space is rendered in green mesh. Note the steric incompatibility between aspartate 59 and the inositol ring of PITPα-bound PtdIns. Both PITPα and Pitpα^{T59D} images were generated with PyMOL 0.99 using the PtdIns-bound PITPα crystal structure as a framework (Protein Data Bank accession number 1UW5) (30).

That *Tg(Pitpα^{T59D})* is transcribed was verified by two lines of evidence. First, reverse transcription PCR using the same primers used for MAMA-PCR detected *Tg(Pitpα^{T59D})* mRNA only in *Tg(Pitpα^{T59D})* mice (Fig. 2D). Second, DNA sequence analysis of the entire *PITPα* cDNA coding sequence generated by reverse transcription of brain mRNA from *PITPα$^{+/0}$;Tg(Pitpα^{T59D})* animals identified a single polymorphism. This polymorphism resulted in the detection of both threonine and aspartate codons at *PITPα* codon 59 [from *PITPα^{+}* and *Pitpα^{T59D}* alleles, respectively (Fig. 2E, left and middle panels)]. The similar magnitudes with which each polymorphism was recorded indicate that *Tg(Pitpα^{T59D})* supports transcriptional expression at levels comparable to those of endogenous *PITPα*.

PtdIns binding/transfer is required for PITPα function in mammals

Standard matings between *PITPα$^{+/0}$;Tg(Pitpα^{T59D})* males and females generated the full complement of expected genotypes. As all PITPα-sufficient progeny exhibited phenotypes indistinguishable from the wild type, irrespective of their *Tg(Pitpα^{T59D})* genotype, we restricted our attention to comparisons of *PITPα$^{+/+}$;Tg(Pitpα^{T59D})*, *Pitpα$^{0/0}$*, and *Pitpα$^{0/0}$;Tg(Pitpα^{T59D})* littermates. Lifespan-monitoring experiments demonstrated that *Tg(Pitpα^{T59D})* expression does not rescue the neonatal and perinatal lethality of otherwise PITPα nullizygous offspring. For *Pitpα$^{0/0}$;Tg(Pitpα^{T59D})* progeny, the rapid onset of postnatal mortality characteristic of PITPα nullizygous mice was on display (**Fig. 3A**). Comparison of *Pitpα$^{0/0}$* and *Pitpα$^{0/0}$;Tg(Pitpα^{T59D})* progeny at P3 and P6 revealed that both strains exhibited the wasting phenotype typical of PITPα nullizygotes. This wasting was associated with dramatic reductions in the contribution of subcutaneous fat to total body mass (data not shown). Additional analyses of *Pitpα$^{0/0}$;Tg(Pitpα^{T59D})* mice demonstrated that these also exhibited the striking hypoglycemia and intestinal and liver microvesicular steatosis disorders that accompany PITPα nullizygosity (**Table 1**). Phenotypic manifestations of the robust neurodegenerative disease characteristic of *Pitpα$^{0/0}$* neonates were also apparent (data not shown). In sum, the *Pitpα$^{0/0}$* and *Pitpα$^{0/0}$;Tg(Pitpα^{T59D})* phenotypes were indistinguishable based on criteria of severity and rate of onset.

Failure of *Tg(Pitpα^{T59D})* to rescue lethality, or the other various pathologies of *Pitpα$^{0/0}$* mice, revealed an intrinsic biological nonfunctionality of Pitpα^{T59D}. Lack of activity was not a consequence of reduced protein expression or stability. Immunoblotting for PITPα in total brain, duodenum, and liver extracts culled from appropriate mouse strains showed that Pitpα^{T59D} levels are comparable to those of PITPα in vivo (Fig. 3C). For final confirmation,

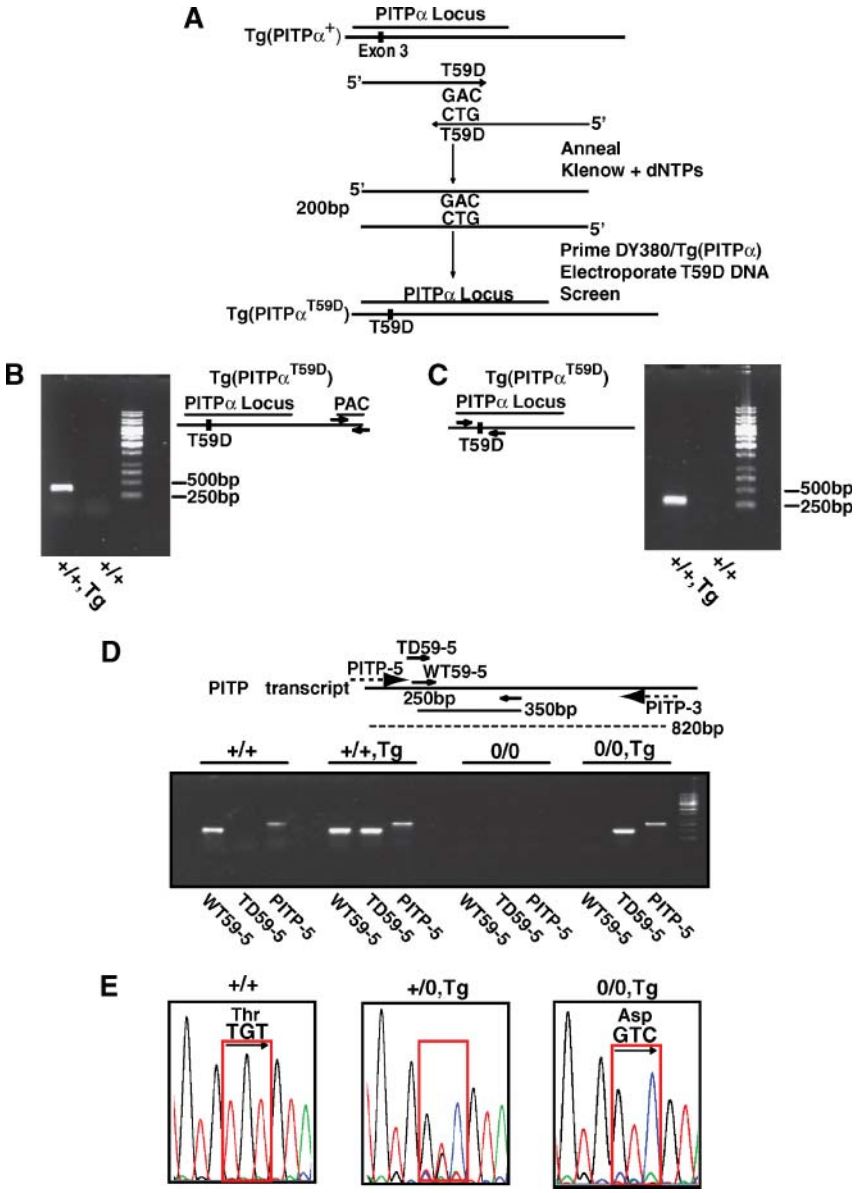

Fig. 2. Generation of mice expressing a PtdIns binding-deficient PITPα. A: P1 artificial chromosome (PAC) mutagenesis strategy. *Tg(PITPα^{+})* represents P1 clone 4232, which contains the entire 76 kb *PITPα^{+}* structural gene. The *Pitpα^{T59D}* missense substitution was introduced into this PAC by recombineering-driven site-directed mutagenesis, as described in Materials and Methods. dNTP, deoxynucleoside triphosphate. B: Diagnosis of *Tg(Pitpα^{T59D})* in mouse genomic DNA. The mutant transgene was detected in candidate transgenic mouse founder lines using a PCR strategy screening for the presence of the PAC vector backbone. Arrows indicate the positions of forward and reverse diagnostic PCR primers that yield a 350 bp product detected exclusively in genomic DNA prepared from founder mice carrying *Tg(Pitpα^{T59D})*. C: Confirmation of *Tg(Pitpα^{T59D})* in candidate transgenic founder lines. Arrows indicate primers used in mismatch amplification mutation assay (MAMA)-PCR analysis (which yields a 300 bp PCR product; left panel) to specifically reveal the *Pitpα^{T59D}* allele. D: *Tg(Pitpα^{T59D})* is actively transcribed. The upper panel illustrates the RT-PCR strategy used to detect transcripts in *Tg(Pitpα^{T59D})* mice. Solid arrows indicate MAMA-PCR primers used to distinguish endogenous *PITPα^{+}* mRNA (WT59-5) transcripts from those of *Pitpα^{T59D}* (TD59-5). In both cases, the diagnostic PCR products are 350 bp. Dashed arrows indicate the forward and reverse PCR primers (PITP-5 and PITP-3) used in RT-PCR assays to reveal full-length *PITPα* transcripts (820 bp product) without distinguishing *PITPα^{+}* transcripts from those of *Pitpα^{T59D}*. The lower panel demonstrates this method. Mouse genotype is indicated at the top and RT-PCR products are identified at the bottom of individual lanes. E: Confirmation that *Pitpα^{T59D}* is properly expressed. Nucleotide sequence analysis of the RT-PCR product generated by the PITP-5/PITP-3 primer combination. The left panel shows the cDNA sequence readout of relevant codons from a *PITPα$^{+/+}$* mouse. The middle and right panels are the corresponding readouts from *PITPα$^{+/0}$,Tg(Pitpα^{T59D})* and *Pitpα$^{0/0}$,Tg(Pitpα^{T59D})* mice, respectively. Genotypes are indicated at the top, and relevant sequences are identified at the top of the red boxes. Corresponding amino acids are listed: Asp, aspartate; Thr, threonine. Note that the *PITPα$^{+/0}$,Tg(Pitpα^{T59D})* reactions reveal sequences derived from both *PITPα^{+}* from *Pitpα^{T59D}* alleles.

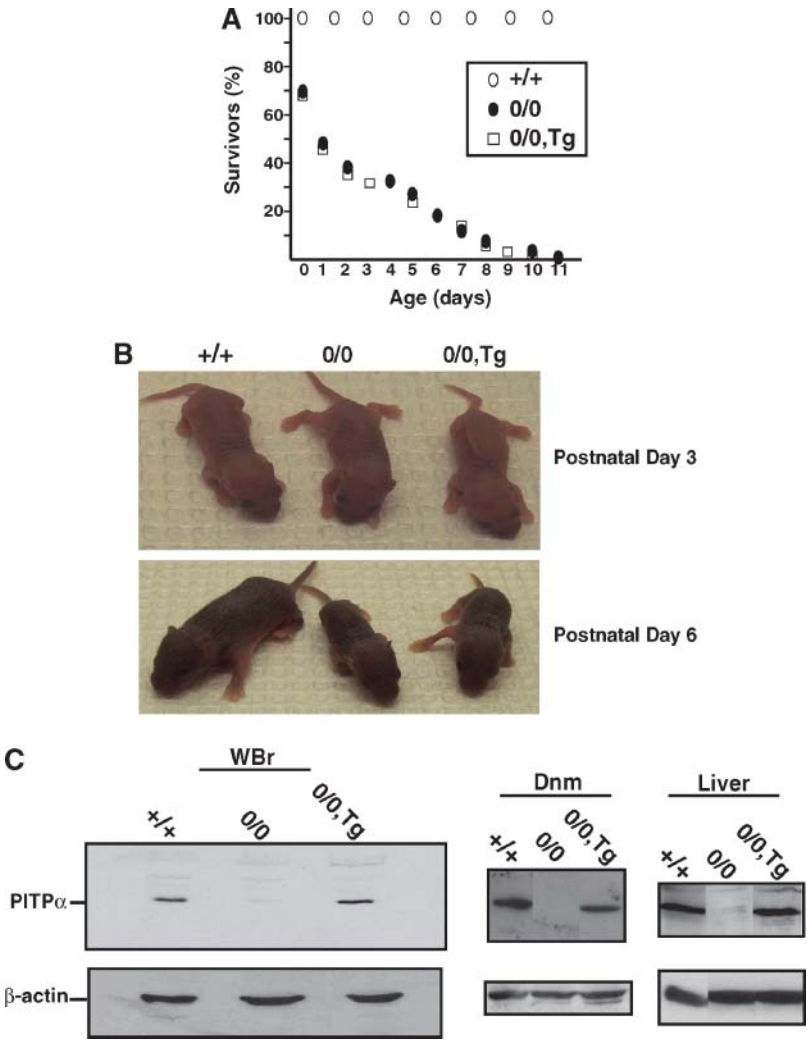

Fig. 3. Pitpα^{T59D} is not a biologically functional protein. A: Lifespans for *PITPα*$^{+/+}$ (open circles), *Pitpα*$^{0/0}$ (closed circles), and *Pitpα*$^{0/0}$*,Tg(Pitpα*^{T59D}*)* (open squares) mice are plotted. The data were obtained from a dedicated pool of 176 mice with a genotypic distribution of 118 *PITPα*$^{+/+}$, 26 *Pitpα*$^{0/0}$, and 32 *Pitpα*$^{0/0}$*, Tg(Pitpα*^{T59D}*)*. B: Images of *PITPα*$^{+/+}$, *Pitpα*$^{0/0}$, and *Pitpα*$^{0/0}$*,Tg(Pitpα*^{T59D}*)* mice taken at the indicated ages. C: *Tg(Pitpα*^{T59D}*)* protein is expressed at physiological levels. Immunoblot analysis of PITPα immunoreactive species from whole brain (WBr), duodenum (Dnm), and liver, collected from P6 littermates of the indicated genotypes, using a PITPα-specific C-terminal polyclonal antibody (top panels). The bottom panels depict the corresponding blots that were stripped and reprobed with a β-actin-specific antibody for purposes of normalization.

mRNA was purified from brains of *Pitpα*$^{0/0}$*;Tg(Pitpα*^{T59D}*)* progeny, and the total brain mRNA fraction was used to template *PITPα* cDNA synthesis. The templating strategy sustained unbiased synthesis of both *PITPα*$^{+}$ and *Pitpα*^{T59D} cDNAs. The open reading frame sequence of PITPα cDNA was then determined. These analyses confirmed Pitpα^{T59D} as the sole detectable PITPα species expressed in *Pitpα*$^{0/0}$*; Tg(Pitpα*^{T59D}*)* mice (Fig. 2E, right panel). We conclude from these experiments that PtdIns binding is essential for PITPα biological activity.

An allelic series for titrating PITPα expression in mice

PITPα-deficient mice elaborate multiple phenotypes. Manifestation of some of these phenotypes is sensitive to amounts of PITPα protein (21, 22). These findings suggest that titration of PITPα function in mice is a viable approach for discerning relationships between the complex phenotypes that accompany PITPα insufficiencies. To this end, we took advantage of the availability of *Pitpα*^{0} and *Pitpα*^{vb} alleles to create a series of murine strains with graded levels of PITPα expression. The *Pitpα*^{vb} allele reduces the expression of wild-type PITPα as a result of the insertion of an IAP element into intronic sequences of the PITPα structural gene (22). Because the *Pitpα*^{0} allele was originally fixed in the 129SVJ genetic background, and the hypomorphic *Pitpα*^{vb} phenotype is sensitive to genetic modifiers (22), *Pitpα*^{0} was incorporated into the C57BL/6J genetic background by serial backcross (see Materials and Methods). The C57BL/6J background elicits the most severe phenotype for the *Pitpα*^{vb} homozygote mice and is

TABLE 1. *Pitpα*^{T59D} is nonfunctional in the mouse

Genotype	Age	Serum Glucose	Plasma TGs	Steatosis Intestine	Mass Liver	
		mM	*mg/dl*			*g*
PITPα$^{+/+}$	P3	4.2 ± 1.1	105.5 ± 12.2			
	P5	8.1 ± 1.5	128.7 ± 7.4	−−−	−−−	3.5 ± 0.4
	P6	8.5 ± 1.3	133.1 ± 9.2			
Pitpα$^{0/0}$	P3	2.3 ± 0.7	62.5 ± 7.5			
	P5	2.1 ± 0.5	56.3 ± 8.8	+++	+++	2.6 ± 0.4
	P6	2.1 ± 0.8	57.9 ± 5.4			
Pitpα$^{0/0}$;*Tg*(*Pitpα*^{T59D})	P3	1.9 ± 0.6	65.4 ± 8.4			
	P5	2.4 ± 0.9	55.7 ± 5.6	+++	+++	2.4 ± 0.3
	P6	2.0 ± 1.1	54.5 ± 6.4			

PITP, phosphatidylinositol transfer protein; TG, triglyceride, +++, severe steatosis. Values represent the averages of values measured for three mice for each age and genotype. Serum glucose values were measured in duplicate for each mouse to give an average value, which was then used to generate the average values reported for each group. Single plasma TG measurements were taken for each mouse, and these values were then averaged to yield the data shown. Serum glucose and plasma TG measurements were performed using the same blood samples collected from each mouse. Steatosis of intestine and liver was monitored by osmium staining of organ sections collected from mice of the indicated age and genotype.

minimized for the *Pitpα*^{vb} genetic modifiers detected in other murine strain backgrounds (22). Comparisons of the morbidity of *Pitpα*$^{0/0}$ offspring as a function of genetic background (C57BL/6J vs. 129SVJ) demonstrated that the lifespans of nullizygotes were very similar in both genetic background contexts (50% mortality at 4.2 ± 1.2 vs. 4.8 ± 0.7 days, respectively).

Standard mating schemes were used to generate C57BL/6J-derived mice harboring *Pitpα*$^{+/+}$, *Pitpα*$^{+/0}$, *Pitpα*$^{vb/vb}$, *Pitpα*$^{vb/0}$, and *Pitpα*$^{0/0}$ allelic combinations. Relative levels of endogenous PITPα in whole brain cytosol extracts were prepared from mice of each genotype and compared by immunoblotting and quantitative ELISA (**Fig. 4A**, **B**). Again, in both experiments, antibodies specific for PITPα were used to avoid confounding issues presented by the highly similar PITPβ isoform in these mice. In that regard, *PITPα*$^{+/+}$, *PITPα*$^{+/vb}$, *PITPα*$^{+/0}$, *Pitpα*$^{vb/vb}$, *Pitpα*$^{vb/0}$, and *Pitpα*$^{0/0}$ mice express ~100, 94, 61, 18, 13, and <3% of wild-type PITPα levels, respectively (Fig. 4B). These data indicate that the titration range for PITPα was a satisfactorily broad one. For purposes of these studies, we focus on *PITPα*$^{+/+}$ and *Pitpα*$^{0/0}$ strains as positive and null controls, respectively, and *Pitpα*$^{vb/vb}$ and *Pitpα*$^{vb/0}$ mice as experimental variables.

Phenotypes of mice with graded reductions in PITPα expression

Analyses of the allelic series emphasized the close correlation between the primary phenotypes of PITPα-deficient animals and levels of PITPα expression. From the perspective of viability, *Pitpα*$^{0/0}$ offspring exhibited a steady mortality rate in the P0 to P11 window. *Pitpα*$^{vb/0}$ animals survived until P19 and then expired precipitously over the next 3 days (**Fig. 5A**). Similarly, and in agreement with previous reports (22, 31), *Pitpα*$^{vb/vb}$ juveniles persisted until P28 and then expired during the next 5 days. No deaths were scored for *PITPα*$^{+/+}$ animals during this period. Indeed, both *PITPα*$^{+/vb}$ and *PITPα*$^{+/0}$ heterozygotes were phenotypically normal in every obvious way throughout their normal lifetime of ~24 months (data not shown). The intermediate lifespan of *Pitpα*$^{vb/0}$ offspring, relative to *Pitpα*$^{0/0}$ and *Pitpα*$^{vb/vb}$ counterparts, extended to other phenotypes. For example, *Pitpα*$^{vb/vb}$ juveniles were afflicted with a whole body tremor whose onset was observed at P18. This onset advanced to P12 for *Pitpα*$^{vb/0}$ mice. Body mass analyses revealed a similar pattern. Whereas a clear distinction in mass was already apparent between *PITPα*$^{+/+}$ and *Pitpα*$^{0/0}$ littermates by P5 (3.3 ± 0.4 vs. 1.9 ± 0.5 g; $P < 0.003$) (Fig. 5B), a significant difference between the average body mass of *PITPα*$^{+/+}$ and *Pitpα*$^{vb/0}$ animals was not scored until P11 (Fig. 5B, C). This difference in mass coincided with onset of the whole body tremor in the *Pitpα*$^{vb/0}$ animals, and it exaggerated rapidly. By P15, *Pitpα*$^{vb/0}$ juveniles embarked on a swift wasting process that persisted until death (Fig. 5B).

Quantitative relationship between PITPα activity and steatosis of intestine and liver

A hallmark pathology of *Pitpα*$^{0/0}$ neonates is a microvesicular steatosis of duodenal enterocytes and liver. The intestinal steatosis reflects the accumulation of dietary fat in enterocytes as a result of defective transport of that material from enterocytes into the circulation. These steatotic phenotypes are proposed to reflect defects in chylomicron biogenesis in enterocytes and lipid processing in the liver, respectively (21). Steatosis is amenable to histological examination by osmium staining of thin tissue sections, and intestinal steatosis is also diagnosed by analytical measurements of postprandial plasma TGs and brain α-tocopherol. Although osmium staining of duodenal and liver tissue sections revealed the expected steatosis in *Pitpα*$^{0/0}$ offspring, clear reductions in enterocytic and hepatic steatosis were observed in *Pitpα*$^{vb/0}$ siblings. No overt steatotic pathologies were apparent in *Pitpα*$^{vb/vb}$ animals relative to wild-type sibling controls (**Fig. 6A**, **B**).

The histological data were consistent with measurements of postprandial plasma TGs and brain α-tocopherol. Regarding plasma TG content, *Pitpα*$^{0/0}$ neonates exhibited ~4-fold reductions in circulating plasma TG relative

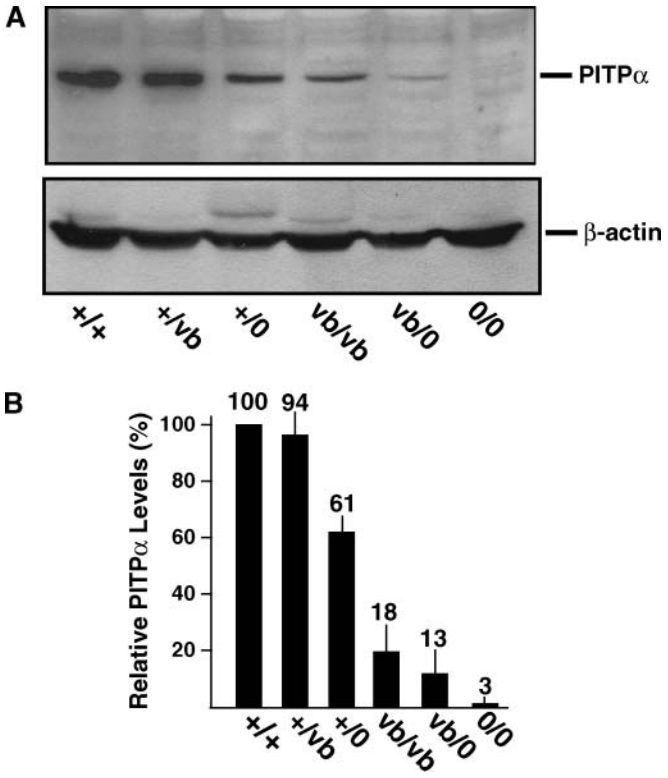

Fig. 4. Quantification of PITPα protein levels in a series of mice harboring various *PITPα* mutant allele combinations. A: Immunoblot analyses of PITPα immunoreactive species from whole brain lysates collected from P8 mice of the indicated genotypes. The top panel presents immunoblot profiles obtained by probing the indicated lysate preparations with a PITPα-specific antibody. The bottom panel represents the same blot stripped and reprobed with a β-actin-specific antibody as a normalization control. B: ELISA analyses of PITPα protein levels from the same whole brain lysate preparations described for A. Results are expressed as PITPα levels relative to $PITP\alpha^{+/+}$ controls (set at 100%) after correction for relative β-actin ELISA values. The values represent averages (plus SD) from triplicate measurements for each of three independent brain samples collected from three mice of each genotype.

to $PITP\alpha^{+/+}$ siblings, whereas $Pitp\alpha^{vb/0}$ mice showed only an ~2-fold reduction in the same parameter. $Pitp\alpha^{vb/vb}$ offspring presented normal circulating plasma TG (Fig. 6C). Similarly, the brain α-tocopherol deficit in $Pitp\alpha^{0/0}$ offspring (0.69 ± 0.31 vs. 2.71 ± 0.45 ng/mg for $PITP\alpha^{+/+}$ siblings) was corrected in $Pitp\alpha^{vb/0}$ and $Pitp\alpha^{vb/vb}$ brain (2.60 ± 0.32 and 2.51 ± 0.56 ng/mg, respectively; Fig. 6D). These data indicate that the intestinal and liver steatosis pathologies manifest themselves only in the face of large (≥90%) reductions in PITPα expression.

Reconstitution of PITPα in small intestine of $Pitp\alpha^{0/0}$ mice

The involvement of PITPα in chylomicron trafficking from nullizygous enterocytes is puzzling, as the affected organelle [endoplasmic reticulum (ER)] is the major intracellular site of lipid synthesis. Moreover, it remains unknown whether this pathology reflects a tissue-autonomous defect and what CRD contributes to the complex disease phenotypes of $Pitp\alpha^{0/0}$ neonates. To this end, a transgene was engineered in which duodenum-specific expression of PITPα cDNA is driven by the intestinal fatty acid binding protein enhancer [$Tg(P_{IFABP}::PITP\alpha)$] (**Fig. 7A**) (see Materials and Methods). Immunoblotting experiments of brain and intestine culled from $PITP\alpha^{+/+}$, $Pitp\alpha^{0/0}$, and $Pitp\alpha^{0/0};Tg(P_{IFABP}::PITP\alpha)$ offspring confirmed that the transgene supports a satisfactory tissue-specific expression of physiologically relevant levels of PITPα (Fig. 7A).

Osmium staining demonstrated that $Pitp\alpha^{0/0};Tg(P_{IFABP}::PITP\alpha)$ offspring were relieved of the intestinal steatosis observed for their $Pitp\alpha^{0/0}$ siblings (Fig. 7B). The rescue-of-steatosis phenotype exhibited tissue specificity, as liver steatosis was not alleviated by $Tg(P_{IFABP}::PITP\alpha)$ (Fig. 7C). In fact, this liver pathology was, if anything, exacerbated. Thin-section electron microscopy confirmed this effect and indicated that the accumulated lipid in $Pitp\alpha^{0/0};Tg(P_{IFABP}::PITP\alpha)$ liver is divided between what appears to be a pool that resides in the ER lumen and a pool that partitions into cytoplasmic lipid droplets (data not shown). Rescue of intestinal steatosis, as scored by histological staining methods, was accompanied by improved transport of chylomicron into the circulation. $Pitp\alpha^{0/0};Tg(P_{IFABP}::PITP\alpha)$ animals exhibited 59.1 ± 10.6% of the serum chylomicron load of their age-matched $PITP\alpha^{+/+}$ controls. Relative to $Pitp\alpha^{0/0}$ animals, whose circulating chylomicron load was just 24.7 ± 8.8% of wild-type levels (**Fig. 8A**), this represented a marked improvement.

Plasma TG and brain α-tocopherol enter the circulation via the chylomicron pathway, and measurements of these components were congruent with the chylomicron data. $Pitp\alpha^{0/0};Tg(P_{IFABP}::PITP\alpha)$ neonates exhibited 59.2 ± 5.9 mg/dl relative to 39.2 ± 6.1 and 138.1 ± 7.9 mg/dl plasma TG for $Pitp\alpha^{0/0}$ and $PITP\alpha^{+/+}$ siblings, respectively (Fig. 8B). Substantial rescue of brain α-tocopherol deficit was similarly registered in $Pitp\alpha^{0/0};Tg(P_{IFABP}::PITP\alpha)$ offspring (3.04 ± 0.72 vs. 1.19 ± 0.22 and 3.99 ± 0.68 ng/mg brain tissue for $Pitp\alpha^{0/0}$ and $PITP\alpha^{+/+}$ littermates, respectively; Fig. 8C). Thus, intestinal steatosis is a tissue-autonomous pathology in $Pitp\alpha^{0/0}$ mice.

Lifespan and body mass measurements indicated that duodenal PITPα expression levied modest improvement in these parameters relative to $Pitp\alpha^{0/0}$ siblings. Although ~75% of the $Pitp\alpha^{0/0}$ offspring expired within the first 3 days after birth, some 80% of their $Pitp\alpha^{0/0};Tg(P_{IFABP}::PITP\alpha)$ siblings survived past this benchmark (**Fig. 9A**). A 75% mortality standard was not reached for the $Pitp\alpha^{0/0};Tg(P_{IFABP}::PITP\alpha)$ neonates until ~8 days after birth. Again, although modest, this represents an effective doubling of the $Pitp\alpha^{0/0}$ lifespan. Body mass measurements also showed measurable increases in weight gain differential for $Pitp\alpha^{0/0};Tg(P_{IFABP}::PITP\alpha)$ and $Pitp\alpha^{0/0}$ neonates (Fig. 9B). For instance, at P7, the respective mass differential was 3.1 ± 0.3 versus 2.3 ± 0.5 g ($P = 0.026$).

PITPα expression and glucose homeostasis

$Pitp\alpha^{0/0}$ neonates are hypoglycemic. This condition is suggested to contribute to the neurodegenerative pathologies and morbidity of mutant animals. Hypoglycemia

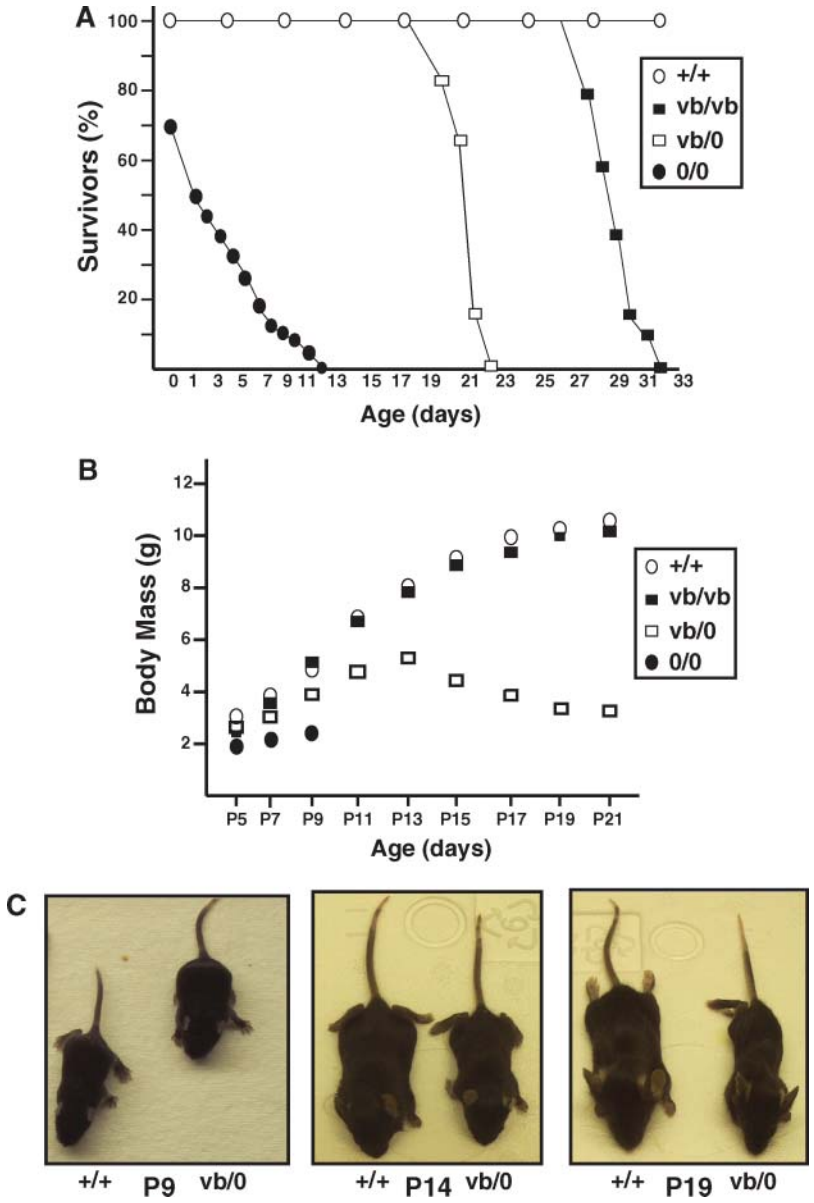

Fig. 5. Phenotyping of mice with graded levels of PITPα protein. A: Lifespan plots for *PITPα*$^{+/+}$ (open circles), *Pitpα*$^{vb/vb}$ (closed squares), *Pitpα*$^{vb/0}$ (open squares), and *Pitpα*$^{0/0}$ (closed circles) are shown. B: Average body masses of *PITPα*$^{+/+}$ (open circles), *Pitpα*$^{vb/vb}$ (closed squares), *Pitpα*$^{vb/0}$ (open squares), and *Pitpα*$^{0/0}$ (closed circles) neonates are plotted in the P5 through P21 age window. Values represent averages over lifespan for progeny derived from four independent litters for each genotype. No *Pitpα*$^{0/0}$ neonates survived past P9 in these dedicated pools of animals. C: Images of P9, P14, and P19 *PITPα*$^{+/+}$ and *Pitpα*$^{vb/0}$ mice (left and right animals, respectively, in each panel).

coincides with pancreatic islet defects, reduced proglucagon expression, and inefficient glycogenolysis (21). Consistent with previous findings, serum glucose was reduced by ~4-fold for *Pitpα*$^{0/0}$ neonates compared with wild-type littermate controls (2.0 ± 0.1 vs. 8.3 ± 0.2 mM; **Fig. 10A**). By contrast, *Pitpα*$^{vb/0}$ neonates exhibited serum glucose levels that were 2.8-fold higher than those of *Pitp*$^{0/0}$ mice (Fig. 10A). This increase was accompanied by the restoration of efficient glycogenolysis in *Pitpα*$^{vb/0}$ animals (data not shown). Although an improvement, those levels were still ~2-fold lower than those of *PITPα*$^{+/+}$ siblings. *PITPα*$^{vb/vb}$ animals exhibited no significant serum glucose deficits relative to wild-type siblings (8.2 ± 0.9 vs. 8.3 ± 0.2 mM, respectively; Fig. 10A). Thus, as was found for the microvesicular steatosis of duodenum and liver, hypoglycemias associated with PITPα defects require manifest reductions in PITPα activity (≥90%).

Specific reconstitution of PITPα expression in the duodenum of *Pitpα*$^{0/0}$ animals [*Pitpα*$^{0/0}$*;Tg(P*$_{IFABP}$*::PITPα)*] also led to an increase in serum glucose, but this too was incomplete. Circulating glucose values approached, but did not meet, those measured for *Pitpα*$^{vb/0}$ mice (3.5 ± 0.1 vs. 5.6 ± 0.8 mM; Fig. 10A). Analyses of serum glucose as a function of age were also informative. All neonates, re-

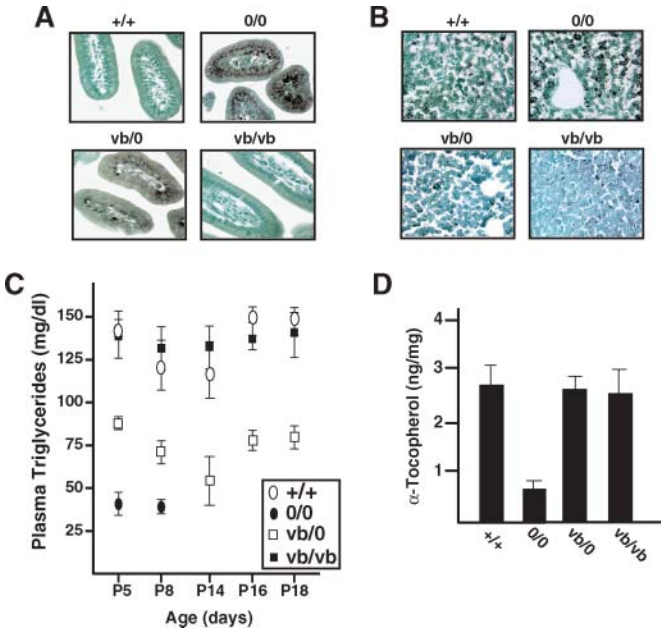

Fig. 6. Chylomicron metabolism in mice with varying levels of PITPα activity. A, B: Osmium staining of intestinal (A) and liver (B) tissue. Panels depict paraffin-embedded, osmium-stained intestinal and liver sections of P8 mice from the indicated genotypes. Steatosis is scored by intensity of osmium staining (black). C: Postprandial plasma triglyceride (TG) levels as a function of age. Plasma was harvested from three age-matched *PITPα*$^{+/+}$ (open circles), *Pitpα*$^{0/0}$ (closed circles), *Pitpα*$^{vb/0}$ (open squares), and *Pitpα*$^{vb/vb}$ (closed squares) animals and measured in triplicate for each mouse at each time point. D: Brain α-tocopherol measurements. Whole brains from age-matched (P6) *PITPα*$^{+/+}$ and *Pitpα*$^{0/0}$ mice, as well as from age-matched (P16) *PITPα*$^{+/+}$, *Pitpα*$^{vb/0}$, and *Pitpα*$^{vb/vb}$ animals, were harvested and corresponding extracts were assayed for α-tocopherol. Measurement averages with SD are shown. Genotypes are listed at bottom.

gardless of genotype, exhibited low blood glucose for the first few days after birth. Although *PITPα*$^{+/+}$ and *Pitpα*$^{vb/vb}$ animals rapidly overcame this condition, *Pitpα*$^{0/0}$ progeny did not (Fig. 10B). *Pitpα*$^{vb/0}$ and *Pitpα*$^{0/0}$*;Tg(P*$_{IFABP}$*::PITPα)* neonates exhibited intermediate increases in serum glucose with age but failed to meet the levels measured for *PITPα*$^{+/+}$ and *Pitpα*$^{vb/vb}$ animals.

PITPα expression and cerebellar neurodegeneration

A hallmark phenotype of *Pitpα*$^{0/0}$ mice is a robust hindbrain and cerebellar inflammatory disease characterized by reactive gliosis in these tissues (21). This pathology is scored by staining for GFAP, a marker for activated astrocytes (**Fig. 11A**). It is suggested that the *Pitpα*$^{0/0}$ cerebellum is particularly sensitive to damage wrought by a systemic energy crisis, such as that precipitated by the CRD and hypoglycemia of *Pitpα*$^{0/0}$ neonates (21). Consistent with this proposal, cerebellar inflammatory disease was substantially alleviated in both *Pitpα*$^{vb/vb}$ and *Pitpα*$^{0/0}$*;Tg(P*$_{IFABP}$*::PITPα)* neonates, as indicated by dramatic reductions in GFAP-positive cells in tissue derived from those mice. By contrast, hindbrain inflammation was not alleviated in either *Pitpα*$^{0/0}$*;Tg(P*$_{IFABP}$*::PITPα)* or *Pitpα*$^{vb/0}$ neonates (Fig. 11B). The persistent hindbrain inflammation presumably reflects some intrinsic fragility/deficit in *Pitpα*$^{0/0}$ hindbrain neurons.

PITPα nullizygosity and efficacy of synaptic transmission

Phosphoinositide signaling plays integral roles in regulating neuronal membrane trafficking (32, 33). This raised the possibility that PITPα regulates the synaptic cycle and that the neurodegenerative disorder of *Pitpα*$^{0/0}$ mice may reflect central deficits in synaptic vesicle release and neurotransmission. To address this issue, basic properties of synaptic transmission in the CA1 region of the hippocampus were examined. The experimental model was justified by two criteria. First, synaptic transmission in the hippocampus is experimentally well characterized. Second, PITPα is highly expressed in hippocampus, as indicated by *LacZ* "knock-in" studies using a *Pitpa::neo/puro/LacZ* splice-trap allele (20). β-Galactosidase staining of P10 *PITPα*$^{+}$*/Pitpa::neo/puro/LacZ* brain sections revealed robust PITPα expression in the hippocampus (**Fig. 12A**).

To compare basal synaptic strengths, age-matched *PITPα*$^{+/+}$ and *Pitpα*$^{0/0}$ mice were used to facilitate hippocampal recordings. In these experiments, input-output curves were generated by varying the stimulation intensity of the Schaffer collateral inputs and recording the slope of the fEPSP. The data indicate that basal synaptic strengths were similar between *PITPα*$^{+/+}$ and *Pitpα*$^{0/0}$ mice (Fig. 12B; $P = 0.949$). To ensure that the relationship between presynaptic neurotransmitter release and the postsynaptic response was unchanged, the amplitudes of the fiber volley (a gauge for presynaptic release) were compared with the fEPSP slope (a gauge for synaptic response magnitude). There were no significant differences between *PITPα*$^{+/+}$ and *Pitpα*$^{0/0}$ mice (Fig. 12C; $P = 0.26$), suggesting that the relationship between presynaptic release and the postsynaptic response was preserved in *Pitpα*$^{0/0}$ animals. To test whether the disruption of normal PITPα activity might alter the probability of presynaptic release and/or the degree of synaptic vesicle mobilization, paired-pulse facilitations across a range of interstimulus intervals were examined. Facilitation did not differ between *PITPα*$^{+/+}$ and *Pitpα*$^{0/0}$ mice, as evaluated from fEPSP slopes (Fig. 12D; $P = 0.35$) or amplitudes (Fig. 12E; $P = 0.81$). These data indicate that mutant CA1 synapses exhibit normal probabilities of neurotransmitter release and normal magnitudes of basal synaptic transmission.

Presynaptic terminals of stratum radiatum neurons were also examined by quantitative morphometry. Defects in the synaptic vesicle cycle should result in abnormal synaptic vesicle densities in such presynaptic terminals. *PITPα*$^{+/+}$ and *Pitpα*$^{0/0}$ littermate mice (four each) were perfused with mixed aldehydes, and brains were collected and embedded. Embedded brains were sectioned through the hippocampus, further processed, and flat-embedded in plastic (34). Blindly coded sample blocks were prepared from the CA1 region of hippocampus, and morphometric analyses focused on synapses in the stratum radiatum. A total of 117 images of randomly selected ter-

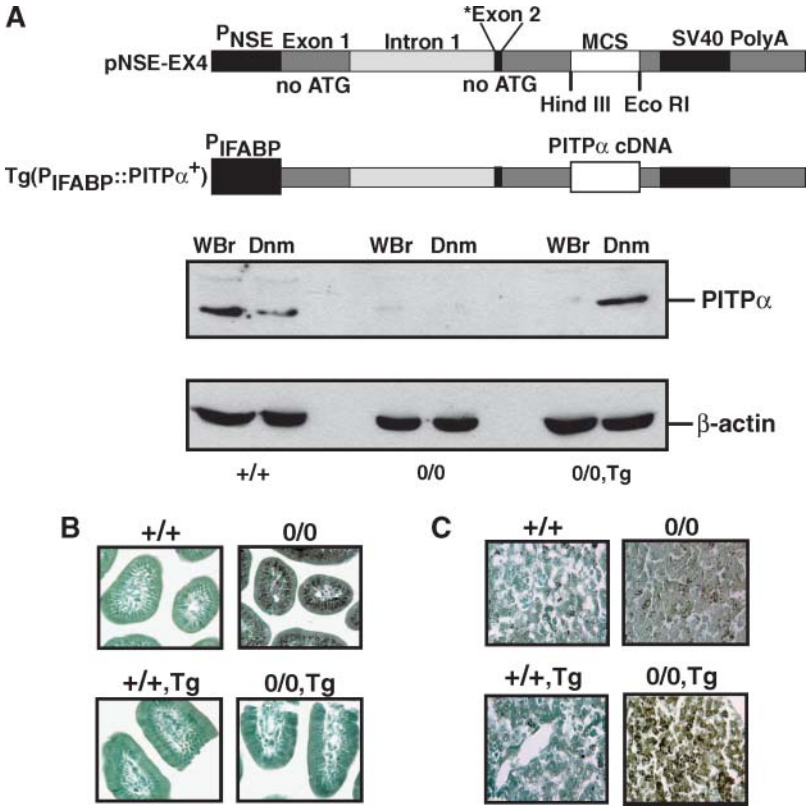

Fig. 7. Intestinal expression of PITPα in *Pitpα*$^{0/0}$ mice. A: The upper panels describe the vectors used to generate *Tg*(P_{IFABP}*::PITPα*$^{+}$). Plasmid pNSE-EX4 was used as an expression vector backbone, and PITPα expression was engineered under the control of the intestinal fatty acid binding protein promoter (P_{IFABP}) (see Materials and Methods). The lower panels show the results of immunoblot analyses using lysates prepared from whole brain (WBr) or duodenum (Dnm) preparations collected from mice of the indicated genotypes. Immunoblot profiles at top monitor PITPα, whereas the immunoblot profiles at bottom record the corresponding β-actin profiles for purposes of normalization. B: Age-matched (P6 littermates) duodenal sections stained with osmium. Genotypes are indicated. C: Liver sections from P6 littermates stained with osmium. Genotypes are indicated.

minals with recognizable synapses were collected, 59 from *PITPα*$^{+/+}$ animals and 58 from *Pitpα*$^{0/0}$ mice. For each terminal, vesicles were counted within a 0.2 μm square area: 0.1 μm lateral to each side from the center of the opposing postsynaptic density and 0.2 μm back into the terminal. The number of vesicles per examined area ranged from 0 to 19. The *PITPα*$^{+/+}$ and *Pitpα*$^{0/0}$ mice averaged 6.4 and 7.7 vesicles per synapse, respectively. Although there were the expected variations in the numbers of vesicles per synapse, no obvious correlation between vesicle number and PITPα status was discerned. Thus, the collective electrophysiological and morphometric data indicate that the synaptic vesicle cycle of *Pitpα*$^{0/0}$ mice is unperturbed, and that neurodegeneration is unlikely to be a consequence of deficits in synaptic transmission.

DISCUSSION

Here, we report a detailed analysis of PITPα function in mice. These studies take advantage of transgenic approaches to achieve three purposes. First, the contribution of PtdIns binding to PITPα function in vivo was evaluated. Second, a series of isogenic mouse strains with graded reductions in PITPα activity was analyzed to examine the relationships between the complex pathologies apparent in *Pitpα*$^{0/0}$ neonates. Third, the consequences of reconstituting PITPα expression solely in the small intestine of *Pitpα*$^{0/0}$ animals were assessed. The conclusions derived from these analyses are as follows: *i*) PtdIns binding activity is essential for PITPα function in the mouse; *ii*) the lifespan of neonatal and juvenile mice is highly sensitive to levels of PITPα; *iii*) large reductions in PITPα expression are required for the elaboration of intestinal and liver steatotic phenotypes and hypoglycemia; *iv*) intestinal steatosis is a tissue-autonomous pathology that is rescued by tissue-specific expression of PITPα; *v*) hindbrain neurodegenerative processes can be largely uncoupled from intestinal/liver steatosis and hypoglycemia, whereas cerebellar inflammatory disease cannot; and *vi*) elimination of PITPα activity has no apparent consequence for synaptic efficacy, even in neurons that normally exhibit high levels of PITPα expression. Together, these data provide the first in vivo demonstration of a meaningful biological role for

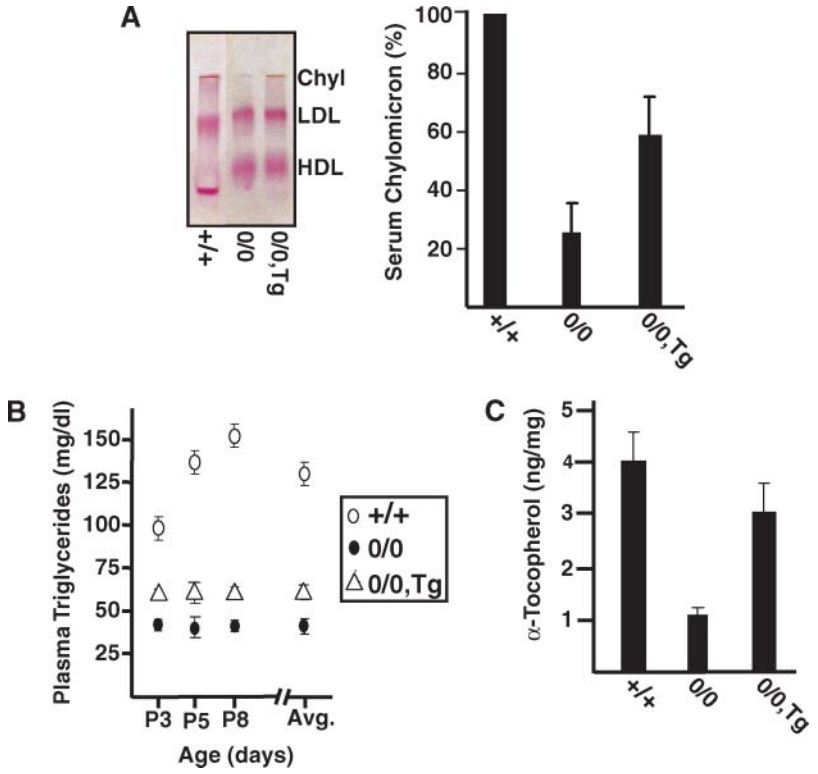

Fig. 8. Chemical analyses of *Pitpα*$^{0/0}$ mice expressing PITPα in the duodenum. A: Postprandial serum chylomicron levels. A Titan lipoprotein agarose gel is shown at left. Genotypes of P5 littermates are indicated, and bands are identified as follows: Chyl, chylomicron; LDL, low density lipoprotein; HDL, high density lipoprotein. The right panel represents quantification (by densitometry) of chylomicron bands from a total of five animals of each indicated genotype. Tg indicates the *Tg(P*$_{IFABP}$*::PITPα*$^{+}$*)* allele. *PITPα*$^{+/+}$ values were uniformly set at 100%, and *Pitpα*$^{0/0}$ and *Pitpα*$^{0/0}$*,Tg(P*$_{IFABP}$*::PITPα*$^{+}$*)* values were related to that benchmark. B: Postprandial plasma TG levels as a function of age. Plasma TGs from three age-matched littermates (as indicated) were measured. Avg. indicates the average of all sample measurements for that particular genotype [*PITPα*$^{+/+}$, open circles; *Pitpα*$^{0/0}$, closed circles; *Pitpα*$^{0/0}$*,Tg(P*$_{IFABP}$*::PITPα*$^{+}$*)*, open triangles]. C: Whole brain α-tocopherol measurements. Four age-matched littermates of each indicated genotype were analyzed. Averaged values with SD are reported. Tg indicates *Tg(P*$_{IFABP}$*::PITPα*$^{+}$*)*.

PtdIns binding by PITPα. The data also bolster the idea that PITPα plays a role in the biogenesis and transport of lipid/lipoprotein cargo from intracellular organelles.

PtdIns binding and PITPα function

Current models suggest that PITPα is devoted primarily to phosphoinositide synthesis, particularly PtdIns-4,5-P_2 synthesis (35–38). Such a role could involve a direct coupling between PITPα and PtdIns 4-OH kinases, in which PITPα presents PtdIns to the enzyme and thereby potentiates its catalytic activity. A more indirect PtdIns delivery mechanism, in which PITPα supplies PtdIns to sites of active signaling from other intracellular membranes (e.g., by PtdIns transfer), is also plausible. Alternatively, PITPα could stimulate PtdIns-4,5-P_2 synthesis by potentiating phospholipase D-mediated hydrolysis of PtdCho [and subsequently stimulating PtdIns-4-phosphate 5-OH kinase activity via the production of the phosphatidic acid hydrolytic product (39)]. The former two models predict a critical role for PtdIns binding by PITPα, whereas the latter model emphasizes PtdCho binding. The finding that physiological levels of expression of Pitpα^{T59D}, as the sole source of PITPα in the mouse, recapitulate phenotypes of *Pitpα*$^{0/0}$ mice, identifies PtdIns binding as an essential functional property of PITPα. This demonstration is most consistent with either PtdIns presentation, or PtdIns transfer, mechanisms for PITPα function in vivo. To distinguish between the presentation and transfer mechanisms, it is necessary to assess the in vivo functionality of mutant PITPα forms with defects in PtdCho binding. Unfortunately, available structural information does not reveal how to generate such PtdCho binding-defective forms of PITPα.

Phenotypic consequences of graded reductions in PITPα expression

Pitpα$^{0/0}$ mice experience a complex disease course of intestinal and hepatic steatosis, hypoglycemia, and inefficient glycogenolysis (stemming from pancreatic insufficiency) and a fulminating spinocerebellar neurodegenerative disease. The neurodegeneration is marked by reactive gliosis of the cerebellum and hindbrain and aponecrotic pathologies in the spinal cord (21). The relationships between these various pathologies is not obvious, however. Analyses of isogenic mouse lines with graded reductions in PITPα

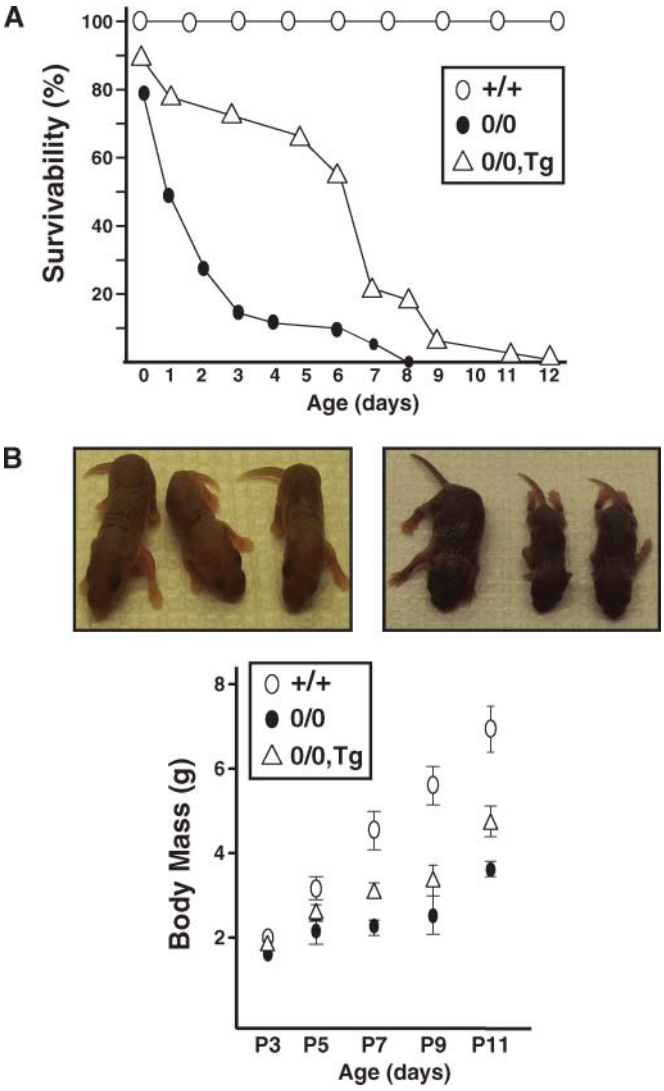

Fig. 9. Characterization of $Pitp\alpha^{0/0}$,$Tg(P_{IFABP}::PITP\alpha^{+})$ mice. A: Lifespan profiles for $PITP\alpha^{+/+}$ (open circles), $Pitp\alpha^{0/0}$ (closed circles), and $Pitp\alpha^{0/0}$,$Tg(P_{IFABP}::PITP\alpha^{+})$ (open triangles) mice are compared. The data were obtained from a dedicated pool of 148 mice with a genotypic distribution of 100 $PITP\alpha^{+/+}$, 21 $Pitp\alpha^{0/0}$, and 27 $Pitp\alpha^{0/0}$,$Tg(P_{IFABP}::PITP\alpha^{+})$. B: Visual characterization and body mass measurements of $Pitp\alpha^{0/0}$,$Tg(P_{IFABP}::PITP\alpha^{+})$ mice. The upper panel shows images of P4 (left) and P7 (right) mice. For each panel, genotypes of mice (from left to right) are $PITP\alpha^{+/+}$, $Pitp\alpha^{0/0}$, and $Pitp\alpha^{0/0}$,$Tg(P_{IFABP}::PITP\alpha^{+})$. The lower panel charts body mass as a function of age for $PITP\alpha^{+/+}$ (open circles), $Pitp\alpha^{0/0}$ (closed circles), and $Pitp\alpha^{0/0}$,$Tg(P_{IFABP}::PITP\alpha^{+})$ (open triangles). Data were obtained from the same dedicated pool of 148 mice used for A. Body mass values were averaged for each genotypic group. SD values are shown.

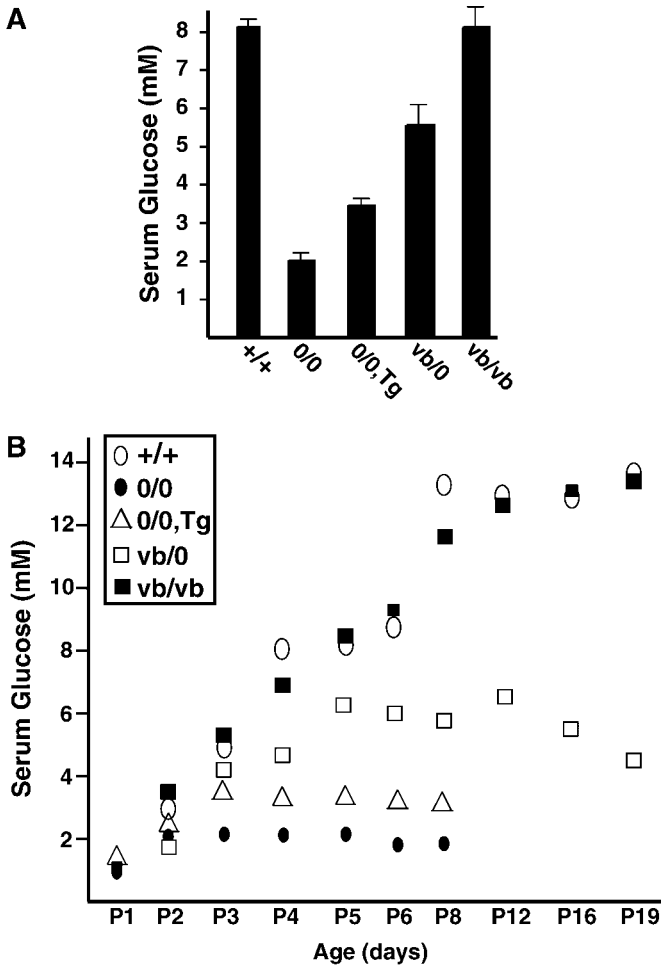

Fig. 10. PITPα levels and glucose homeostasis. A: Average serum glucose values measured from age-matched (P4–P6) $PITP\alpha^{+/+}$, $Pitp\alpha^{0/0}$, $Pitp\alpha^{0/0}$,$Tg(P_{IFABP}::PITP\alpha^{+})$, $Pitp\alpha^{vb/0}$, and $Pitp\alpha^{vb/vb}$ mice. The genotypes are indicated at bottom. B: Serum glucose levels as a function of age. $PITP\alpha^{+/+}$ (open circles), $Pitp\alpha^{0/0}$ (closed circles), $Pitp\alpha^{0/0}$,$Tg(P_{IFABP}::PITP\alpha^{+})$ (open triangles), $Pitp\alpha^{vb/0}$ (open squares), and $Pitp\alpha^{vb/vb}$ (closed squares) serum glucose were determined at the indicated ages. No $Pitp\alpha^{0/0}$ or $Pitp\alpha^{0/0}$,$Tg(P_{IFABP}::PITP\alpha^{+})$ measurements were available beyond P8, as no animals survived past this threshold. Data were obtained from triplicate determinations from each of three mice of each genotype at each time point. The serum glucose values were quite constant for $Pitp\alpha^{0/0}$ and $Pitp\alpha^{0/0}$,$Tg(P_{IFABP}::PITP\alpha^{+})$ mice in the P3–P8 time window (2.3 ± 0.5 vs. 3.8 ± 0.6 mM, respectively), and these differences were significant ($P < 0.0002$).

expression clarify some of these relationships. First, it is clear that the hindbrain inflammatory and spinal cord neurodegenerative diseases are intrinsic pathologies of PITPα-insufficient mice, as these can be uncoupled from intestinal/liver steatosis and hypoglycemia. This is most apparent in the case of $Pitp\alpha^{vb/vb}$ mice, which express ~20% of wild-type levels of PITPα activity. $Pitp\alpha^{vb/vb}$ animals suffer from both hindbrain and spinal cord neurodegeneration (22, 31) but fail to exhibit any symptoms of overt intestinal/liver steatosis or hypoglycemia. By contrast, both intestinal/liver steatosis and hypoglycemia are apparent only in mice in which PITPα activity is reduced by ⩾90% (i.e., $Pitp\alpha^{0/0}$ and $Pitp\alpha^{vb/0}$ lines). Moreover, the severities of the respective pathologies are closely correlated. $Pitp\alpha^{vb/0}$ mice exhibit a less severe intestinal/liver steatosis than $Pitp\alpha^{0/0}$ siblings. $Pitp\alpha^{vb/0}$ mice also show a significantly reduced hypoglycemia. These data are consistent with the view that the hypoglycemia of PITPα-insufficient mice is secondary to intestinal/hepatic lipid transport defects.

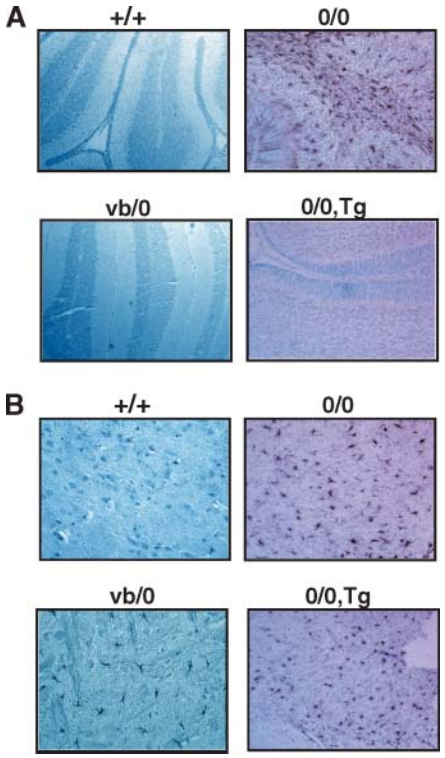

Fig. 11. Cerebellar neurodegeneration and PITPα expression. Sagittal sections of cerebellum (A) or hindbrain (B) were infiltrated with paraffin and stained for glial fibrillary acidic protein. Genotypes are indicated; Tg indicates the *Tg(P$_{IFABP}$::PITPα^{+})* allele. Tissue sections were from P8 animals except for *Pitpα$^{vb/0}$* mice, for which P14 animals were used. These ages were chosen on the basis that neurodegenerative disease had progressed to the obvious whole body tremor stage.

Reconstitution of PITPα expression in small intestine

The intestinal steatosis of *Pitpα$^{0/0}$* mice is an intriguing phenotype. Its characteristics are consistent with a defect in the biogenesis/transport of chylomicrons from the enterocyte ER (21). Indeed, the steatotic condition (and its consequences) resemble those of human CRD (40, 41). One underlying mechanism for human CRD stems from defects in a specific isoform of the Sar1-GTPase (42). This raises the attractive possibility that specific components of the COPII ER vesicle-budding machinery are dedicated to the biogenesis of vesicles containing atypical cargo, such as chylomicrons.

A role for PITPα in chylomicron biogenesis/trafficking is unanticipated, as it is not obvious why such a protein would be required for ER transport processes, given that the ER is the major site of lipid synthesis in cells. Moreover, the ER is not an acknowledged site of phosphoinositide signaling. Yet, the available data indicate a connection between PITPα function and chylomicron metabolism. Specific defects in PITPα PtdIns binding are sufficient to elicit CRD-like symptoms in Pitpα^{T59D}-expressing mice. Moreover, reexpression of PITPα in the small intestine of *Pitpα$^{0/0}$* mice alleviates the steatotic phenotype of this organ and partially rescues the biochemical defects associated with CRD. *Pitpα$^{0/0}$;Tg(P$_{IFABP}$::PITPα)* neonates also exhibit increased plasma TG levels, increases in the quantities of circulating chylomicrons, and increased brain α-tocopherol levels (a vitamin whose transport into the circulation is dependent on the chylomicron pathway) relative to *Pitpα$^{0/0}$* controls. The rescue experiment additionally identifies the intestinal steatosis as a tissue-autonomous pathology in *Pitpα$^{0/0}$* mice.

Although reconstitution of PITPα expression in the small intestine does have discernible effects, it nonetheless supports only a modest rescue of plasma TG deficits and hypoglycemia and only modest increases in the lifespan of transgenic *Pitpα$^{0/0}$* animals. Exacerbated liver steatosis is observed in these mice, however. As chylomicron remnants are taken up by the liver, remodeled, and reexported as VLDL particles, we suggest that defects in lipoprotein processing/biogenesis in *Pitpα$^{0/0}$* liver significantly neutralize the benefits realized by rescue of the intestinal steatosis. These data suggest a role for PITPα in the hepatic lipoprotein biogenesis/transport pathway, a reasonable possibility given that the pathways for lipoprotein biogenesis and transport are similar in the small intestine and the liver (43–45). We predict that reconstitution of PITPα expression in both the small intestine and the liver of a *Pitpα$^{0/0}$* mouse will yield what is a symptomatically *Pitpα$^{vb/vb}$* mouse.

Differential causes of neurodegenerative disease

It was previously proposed that neonatal *Pitpα$^{0/0}$* cerebellum is especially susceptible to injury because its program of robust cell proliferation is incompatible with the hypoglycemic environment presented by the nullizygous mouse (21). The results reported here are consistent with this idea. Both *Pitpα$^{vb/0}$* and *Pitpα$^{0/0}$;Tg(P$_{IFABP}$::PITPα)* neonates are substantially free of the dramatic reactive gliosis that characterizes their *Pitpα$^{0/0}$* siblings. This is a telling result in the context of the *Pitpα$^{0/0}$;Tg(P$_{IFABP}$::PITPα)* mouse, as the cerebellum fails to express PITPα yet is spared the normal course of inflammatory disease by PITPα expression in the small intestine. Consistent with these data, cerebellar granule cells cultured from *PITPα$^{+/+}$* and *Pitpα$^{0/0}$* neonates show no obvious differences in vigor when cultured in vitro (i.e., under culture conditions in which defects associated with systemic lipid transport and hypoglycemia are irrelevant; data not shown).

As hindbrain and spinal cord defects are not alleviated by PITPα expression in the duodenum, these pathologies reflect intrinsic neuronal defects of PITPα-insufficient mice. These pathologies do not stem from deficiencies in the synaptic vesicle cycle, given that synaptic function is not adversely affected by genetic ablation of PITPα activity in hippocampal neurons. Whether these intrinsic defects reflect improper neuronal development and defects in proper path finding (46) or some other signaling defect(s) remains to be determined.

This work was supported by National Institutes of Health Grant NS-37723 (to V.A.B.). B.D.P. was supported by the Whitehall Foundation. The authors thank G. Grossman, H. Mekheel, and

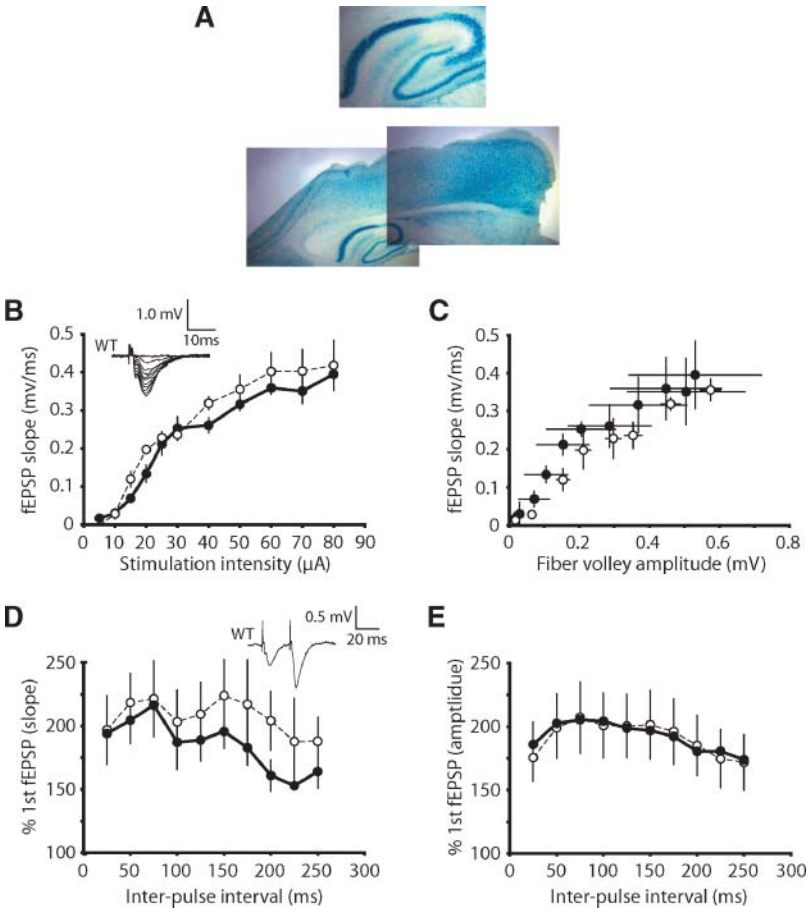

Fig. 12. Synaptic transmission is not affected by PITPα defects. A: PITPα is highly expressed in the hippocampus. At bottom is a representative montage of two merged sections of a sagittal brain slice from a *PITPα*$^{+}$*/Pitpα::neo/puro/LacZ* mouse (P10) stained for β-galactosidase activity. β-Galactosidase expression, driven from the endogenous *PITPα* enhancer, is particularly robust in the hippocampus. The hippocampus region is shown at higher magnification in the top panel. B: Summary input-output curves of field excitatory postsynaptic potentials (fEPSPs) recorded in CA1 of the hippocampus and evoked by Schaffer collateral stimulation. The input-output relationship is similar in *PITPα*$^{+/+}$ and *Pitpα*$^{0/0}$ mice (open and closed circles, respectively). Sample sizes were n = 4 each for *PITPα*$^{+/+}$ and *Pitpα*$^{0/0}$ animals. The waveform depicts a sample input-output recording from a *PITPα*$^{+/+}$ mouse. C: Comparison of fiber volley amplitude to the fEPSP slope in *PITPα*$^{+/+}$ and *Pitpα*$^{0/0}$ mice (open and closed circles, respectively). The similar curves between the two groups suggest that the relationship between presynaptic release and postsynaptic response is unchanged in PITPα nullizygous mice. Sample sizes were n = 4 each for *PITPα*$^{+/+}$ and *Pitpα*$^{0/0}$ animals. D: Paired-pulse facilitation of the fEPSP responses is similar in *PITPα*$^{+/+}$ and *Pitpα*$^{0/0}$ mice (open and closed circles, respectively), indicating that elimination of PITPα activity fails to alter the probability of neurotransmitter release. The slope of the second response is plotted as a percentage of the slope of the first response. The waveform depicts a representative paired-pulse response recorded from a *PITPα*$^{+/+}$ mouse. Sample sizes were n = 5 each for *PITPα*$^{+/+}$ and *Pitpα*$^{0/0}$ mice. E: Same as D except that the fEPSP amplitude was measured instead of the slope. Sample sizes were n = 5 *PITPα*$^{+/+}$ and n = 6 *Pitpα*$^{0/0}$ mice, respectively.

J. de Marchena for valuable technical assistance and Margaret Ryan for help with Fig. 1. The authors also acknowledge the services of the University of North Carolina Lineberger Comprehensive Cancer Center Genome Analysis and Nucleic Acids Core Facilities, and Tammy Elliott and Melinda Beck from the University of North Carolina Clinical Nutrition Research Center (supported by National Institutes of Health Grant DK-56350). Particular thanks are extended to Kris Phend and Richard Weinberg (University of North Carolina) for quantitative morphometry data and to JrGang Cheng of the University of North Carolina Neuroscience Center Bacterial Artificial Chromosome Engineering Core Facility for reagents and helpful advice.

REFERENCES

1. Simons, K., and E. Ikonen. 1997. Functional rafts in cell membranes. *Nature.* **387:** 569–572.
2. Kurzchalia, T. V., and R. G. Parton. 1999. Membrane microdomains and caveolae. *Curr. Opin. Cell Biol.* **11:** 424–431.
3. Fujiwara, T., K. Ritchie, H. Murakoshi, K. Jacobson, and A. Kusumi. 2002. Phospholipids undergo hop diffusion in compartmentalized cell membrane. *J. Cell Biol.* **157:** 1071–1082.
4. Malínská, K., J. Malínsk, M. Opekarová, and W. Tanner. 2003. Visualization of protein compartmentation within the plasma membrane of living yeast cells. *Mol. Biol. Cell* **14:** 4427–4436.
5. McLaughlin, S., and D. Murray. 2005. Plasma membrane phosphoinositide organization by protein electrostatics. *Nature.* **438:** 605–611.

6. Routt, S. M., M. M. Ryan, K. Tyeryar, K. Rizzieri, C. Mousley, O. Roumanie, P. Brennwald, and V. A. Bankaitis. 2005. Nonclassical PITPs activate PLD via the Stt4p PtdIns-4-kinase and modulate late stages of exocytosis in vegetative yeast. *Traffic.* **6:** 1157–1172.
7. Ile, K. E., G. Schaaf, and V. A. Bankaitis. 2006. Phosphatidylinositol transfer proteins and cellular nanoreactors for lipid signaling. *Nat. Chem. Biol.* **2:** 576–583.
8. Phillips, S. E., P. Vincent, K. Rizzieri, G. Schaaf, E. A. Gaucher, and V. A. Bankaitis. 2006. The diverse biological functions of phosphatidylinositol transfer proteins in eukaryotes. *Crit. Rev. Biochem. Mol. Biol.* **41:** 1–28.
9. Sha, B. D., S. E. Phillips, V. A. Bankaitis, and M. Luo. 1998. Crystal structure of the *Saccharomyces cerevisiae* phosphatidylinositol transfer protein. *Nature.* **391:** 506–510.
10. Yoder, M. D., L. M. Thomas, J. M. Tremblay, R. L. Oliver, L. R. Yarbrough, and G. M. Helmkamp, Jr. 2001. Structure of a multifunctional protein. Mammalian phosphatidylinositol transfer protein complexed with phosphatidylcholine. *J. Biol. Chem.* **276:** 9246–9252.
11. Hsuan, J., and S. Cockcroft. 2001. The PITP family of phosphatidylinositol transfer proteins. *Genome Biol.* **2:** 3011.1–3011.8.
12. Allen-Baume, V., B. Segui, and S. Cockcroft. 2002. Current thoughts on the phosphatidylinositol transfer protein family. *FEBS Lett.* **531:** 74–80.
13. Dickeson, S. K., C. N. Lim, G. T. Schuyler, T. P. Dalton, G. M. Helmkamp, Jr., and Y. R. Yarbrough. 1989. Isolation and sequence of cDNA clones encoding rat phosphatidylinositol transfer protein. *J. Biol. Chem.* **264:** 16557–16564.
14. Tanaka, S., and K. Hosaka. 1994. Cloning of a cDNA encoding a second phosphatidylinositol transfer protein from rat brain by complementation of the yeast sec14 mutation. *J. Biochem.* **115:** 981–984.
15. De Vries, K. J., A. A. Heinrichs, E. Cunningham, F. Brunink, J. Westerman, P. J. Somerharju, S. Cockcroft, K. W. Wirtz, and G. T. Snoek. 1995. An isoform of the phosphatidylinositol-transfer protein transfers sphingomyelin and is associated with the Golgi system. *Biochem. J.* **310:** 643–649.
16. Fullwood, Y., M. dos Santos, and J. J. Hsuan. 1999. Cloning and characterization of a novel human phosphatidylinositol transfer protein, rdgBβ. *J. Biol. Chem.* **274:** 31553–31558.
17. Phillips, S. E., K. E. Ile, M. Boukhelifa, R. P. Huijbregts, and V. A. Bankaitis. 2006. Specific and nonspecific membrane-binding determinants cooperate in targeting phosphatidylinositol transfer protein beta-isoform to the mammalian trans-Golgi network. *Mol. Biol. Cell.* **17:** 2498–2512.
18. Morgan, C. P., V. Allen-Baume, M. Radulovic, M. Li, A. Skippen, and S. Cockcroft. 2006. Differential expression of a C-terminal splice variant of PITPb lacking the constitutive-phosphorylated Ser262 that localizes to the Golgi compartment. *Biochem. J.* **398:** 411–421.
19. De Vries, K. J., J. Westerman, P. I. Bastiaens, T. M. Jovin, K. W. Wirtz, and G. T. Snoek. 1996. Fluorescently labeled phosphatidylinositol transfer protein isoforms (alpha and beta), microinjected into fetal bovine heart endothelial cells, are targeted to distinct intracellular sites. *Exp. Cell Res.* **227:** 33–39.
20. Alb, J. G., Jr., S. E. Phillips, K. Rostand, X. Cui, J. Pinxteren, L. Cotlin, T. Manning, S. Guo, J. D. York, H. Sontheimer, et al. 2002. Genetic ablation of phosphatidylinositol transfer protein function in murine embryonic stem cells. *Mol. Biol. Cell.* **13:** 739–754.
21. Alb, J. G., Jr., J. D. Cortese, S. E. Phillips, R. L. Albin, T. R. Nagy, B. A. Hamilton, and V. A. Bankaitis. 2003. Mice lacking phosphatidylinositol transfer protein-α exhibit spinocerebellar degeneration, intestinal and hepatic steatosis, and hypoglycemia. *J. Biol. Chem.* **278:** 33501–33518.
22. Hamilton, B. A., D. J. Smith, K. L. Mueller, A. W. Kerrebrock, R. T. Bronson, V. van Berkel, M. J. Daly, L. Kruglyak, M. O. Reeve, J. L. Nemhauser, et al. 1997. The vibrator mutation causes neurodegeneration via reduced expression of PITP alpha: positional complementation cloning and extragenic suppression. *Neuron.* **18:** 711–722.
23. Forss-Petter, S., P. E. Danielson, S. Catsicas, E. Battenberg, J. Price, M. Nerenberg, and J. G. Sutcliffe. 1990. Transgenic mice expressing beta-galactosidase in mature neurons under neuron-specific enolase promoter control. *Neuron.* **5:** 187–197.
24. Rottman, J. N., and J. I. Gordon. 1993. Comparison of the patterns of expression of rat intestinal fatty acid binding protein/human growth hormone fusion genes in cultured intestinal epithelial cell lines and in the gut epithelium of transgenic mice. *J. Biol. Chem.* **268:** 11994–12002.
25. Lee, E-C., D. Yu, J. de Velasco, L. Tessarollo, D. Swing, D. Court, N. Jenkins, and N. Copeland. 2001. A highly efficient *Escherichia coli*-based chromosome engineering system adapted for recombinogenic targeting and subcloning of BAC DNA. *Genomics.* **73:** 56–65.
26. Liu, P., N. Jenkins, and N. Copeland. 2003. A highly efficient recombineering-based method for generating conditional knockout mutations. *Genome Res.* **13:** 476–484.
27. Luna, L. 1968. Manual of Histological Staining Methods of the Armed Forces Institute of Pathology. Armed Forces Institute of Pathology. The Blakiston Division, McGraw-Hill Book Company, New York. 143–145.
28. Passonneau, J. V., and V. R. Lauderdale. 1974. A comparison of three methods of glycogen measurement in tissues. *Anal. Biochem.* **60:** 405–412.
29. Alb, J. G., Jr., A. Gedvilaite, R. T. Cartee, H. B. Skinner, and V. A. Bankaitis. 1995. Mutant rat phosphatidylinositol/phosphatidylcholine transfer proteins specifically defective in phosphatidylinositol transfer: implications for the regulation of phosphatidylinositol transfer activity. *Proc. Natl. Acad. Sci. USA.* **92:** 8826–8830.
30. Tilley, S. J., A. Skippen, J. Murray-Rust, P. M. Swigart, A. Stewart, C. P. Morgan, S. Cockcroft, and N. Q. McDonald. 2004. Structure-function analysis of phosphatidylinositol transfer protein alpha bound to human phosphatidylinositol. *Structure.* **12:** 317–326.
31. Weimar, W. R., P. W. Lane, and R. L. Sidman. 1982. Vibrator (vb): a spinocerebellar system degeneration with autosomal recessive inheritance in mice. *Brain Res.* **251:** 357–364.
32. Cremona, O., G. Di Paolo, M. R. Wenk, A. Luthi, W. T. Kim, K. Takei, L. Daniell, Y. Nemoto, S. B. Shears, R. A. Flavell, et al. 1999. Essential role for phosphoinositide metabolism in synaptic vesicle recycling. *Cell.* **99:** 179–188.
33. Grishanin, R. N., J. A. Kowalchyk, V. A. Klenchin, K. Ann, C. A. Earles, E. R. Chapman, R. R. Gerona, and T. F. Martin. 2004. CAPS acts at a prefusion step in dense-core vesicle exocytosis as a PIP2 binding protein. *Neuron.* **43:** 551–562.
34. Phend, K. D., A. Rustioni, and R. J. Weinberg. 1995. An osmium-free method of Epon embedment that preserves both ultrastructure and antigenicity for post-embedding immunocytochemistry. *J. Histochem. Cytochem.* **43:** 283–292.
35. Cleves, A. E., T. McGee, and V. A. Bankaitis. 1991. Phospholipid transfer proteins: a biological debut. *Trends Cell Biol.* **1:** 31–34.
36. Wirtz, K. W. A. 1991. Phospholipid transfer proteins. *Annu. Rev. Biochem.* **60:** 73–99.
37. Hay, J. C., and T. F. J. Martin. 1993. Phosphatidylinositol transfer protein is required for ATP-dependent priming of Ca^{2+}-activated secretion. *Nature.* **366:** 572–575.
38. Currie, R. A., B. M. G. Macleod, and P. C. Downes. 1997. The lipid transfer activity of phosphatidylinositol transfer protein is sufficient to account for enhanced phospholipase C activity in turkey erythrocyte ghosts. *Curr. Biol.* **7:** 184–190.
39. Liscovitch, M., V. Chalifa, P. Pertile, C-S. Chen, and L. C. Cantley. 1994. Novel function of phosphatidylinositol-4,5-bisphosphate as a cofactor for brain phospholipase D. *J. Biol. Chem.* **269:** 21403–21406.
40. Levy, E., Y. Marcel, R. J. Deckelbaum, R. Milne, G. Lepage, E. Seidman, M. Bendayan, and C. C. Roy. 1987. Intestinal apoB synthesis, lipids and lipoproteins in chylomicron retention disease. *J. Lipid Res.* **28:** 1263–1274.
41. Aguglia, U., G. Annesi, G. Pasquinelli, P. Spadafora, A. Gambardella, F. Annesi, A. A. Pasqua, F. Cavalcanti, L. Crescibene, A. Bagala, et al. 2000. Vitamin E deficiency due to chylomicron retention disease in Marinesco-Sjogren syndrome. *Ann. Neurol.* **47:** 260–264.
42. Jones, B., E. L. Jones, S. A. Bonney, H. N. Patel, A. R. Mesenkamp, S. Eichenbaum-Voline, M. Rudling, U. Myrdal, G. Annesi, S. Naik, et al. 2003. Mutations in a Sar1 GTPase of COPII vesicles are associated with lipid absorption disorders. *Nat. Genet.* **34:** 29–31.
43. Davis, R. A. 1999. Cell and molecular biology of the assembly and secretion of apolipoprotein B-containing lipoproteins by the liver. *Biochim. Biophys. Acta.* **1440:** 1–31.
44. Olofsson, S. O., L. Asp, and J. Bòren. 1999. The assembly and secretion of apolipoprotein B-containing lipoproteins. *Curr. Opin. Lipidol.* **10:** 341–346.
45. Hussain, M. M., J. Shi, and P. Dreizen. 2003. Microsomal triglyceride transfer protein and its role in apoB-lipoprotein assembly. *J. Lipid Res.* **44:** 22–32.
46. Xie, Y., Y. Q. Ding, Y. Hong, Z. Feng, S. Navarre, C. X. Xi, X. J. Zhu, C. L. Wang, S. L. Ackerman, D. Kozlowski, et al. 2005. Phosphatidylinositol transfer protein-alpha in netrin-1-induced PLC signalling and neurite outgrowth. *Nat. Cell Biol.* **7:** 1124–1132.